Transient Synchronous Stability Analysis of PMSG Grid-Connected System Considering Transient Switching Control Under Severe Faults

Yayao Zhang and Meng Zhan, *Senior Member, IEEE*

***Abstract*—Transient switching control (TSC) of renewable equipment under severe faults makes transient characteristics of new-type power systems much more complicated. Although most of recent studies focused on the during-fault stage under low voltage ride through of grid-connected converters or detailed electromagnetic transient simulations, a unified understanding of entire transient process of permanent magnet synchronous generator (PMSG) grid-connected system is still lacking. Therefore, based on the TSC schemes of PMSG, this article considers the switching dynamical effects in detail, divides the transient process into four distinctive stages: prefault, during-fault, early postfault, and late postfault, and establishes the corresponding mechanism models with the associated machine–network interface relations for each stage. Furthermore, the influence of major parameters on the transient stability is studied, including the infinite-bus voltage dip depth and grid-side converter active current on the during-fault stage, and the active current climbing rate on the early postfault stage. It is also found that the large-disturbance stability on the sole during-fault stage is only a sufficient condition, but not a necessary condition, and actually the system after all four sequential stages can be stable under wider parameter regions. These findings are supported by wide numerical and experimental verification, and could provide a theoretical basis for transient synchronous stability analysis of PMSG grid-connected system.**

***Index Terms*—Low voltage ride through (LVRT), permanent magnet synchronous generator (PMSG), stable region, transient switching control (TSC), transient synchronous stability.**

NOMENCLATURE

PMSG	Permanent magnet synchronous generator.
SG	Synchronous generator.
LVRT	Low voltage ride through.
EAC	Equal area criterion.
TSC	Transient switching control.
PLL	Phase-locked loop.
VSC	Voltage source converter.
CCT	Critical clearing time.
MSC	Machine-side converter.
GSC	Grid-side converter.
AIC	Additional inertia control.
RSC	Rotor speed control.
ACC	AC current control.
DVC	DC-link voltage control.
TVC	Terminal voltage control.
DAE	Differential-algebraic equation.
SCR	Short-circuit ratio.
UEP	Unstable equilibrium point.
θ_{pll}	PLL output angle in three-phase stationary abc reference frame.
φ_{pll}	PLL output angle in xy common reference frame.
θ_t	Terminal voltage angle in xy common reference frame.
P_{in}	Input mechanical power of PMSG.
ψ_r	Rotor flux of PMSG.
P_m, P_e	MSC and GSC output electromagnetic powers, respectively.
$\omega_g, \omega_{\text{pll}}, \omega_r$	xy common reference frame frequency, PLL output frequency, and PMSG rotor speed, respectively.
$i_{\text{sq}}, i_{\text{int}}$	MSC output current in q coordinate and additional inertia control output current, respectively.
i_d, i_q	GSC output currents in d and q coordinates, respectively.
U_t, U_g	Terminal voltage and infinite-bus voltage, respectively.
u_{tq}, u_{tq}	Terminal voltage in d and q coordinates, respectively.
L_g, L_f	Line and filter inductances, respectively.
P'_m, P'_e	Equivalent mechanical power and equivalent electromagnetic power, respectively.
$k_{p,\text{rsc}}$, $k_{i,\text{rsc}}$	Proportional and integral parameters of RSC, respectively.
$k_{p,\text{pll}}$, $k_{i,\text{pll}}$	Proportional and integral parameters of PLL, respectively.
$k_{p,\text{tvc}}$, $k_{i,\text{tvc}}$	Proportional and integral parameters of TVC, respectively.
K_f, T_f	Parameters of AIC.
k_{ramp}	Active current climbing rate.
t_f, t_c	Fault occurrence time and fault clearing time, respectively.

Received 2 September 2024; revised 21 November 2024; accepted 31 December 2024. Date of publication 3 January 2025; date of current version 26 February 2025. This work was supported by the National Natural Science Foundation of China under Grant U22B6008. Recommended for publication by Associate Editor A. M. Bazzi. *(Corresponding author: Meng Zhan.)*

The authors are with the State Key Laboratory of Advanced Electromagnetic Engineering and Technology, Hubei Electric Power Security and High Efficiency Key Laboratory, School of Electrical and Electronic Engineering, Huazhong University of Science and Technology, Wuhan 430074, China (e-mail: zhanmeng@hust.edu.cn; zhang_yayao@hust.edu.cn).

Color versions of one or more figures in this article are available at https://doi.org/10.1109/TPEL.2025.3525746.

Digital Object Identifier 10.1109/TPEL.2025.3525746

Subscripts

1, 2, 3, 4 Stages 1, 2, 3, and 4, for prefault, during-fault, early postfault, and late postfault, respectively.

I. Introduction

IN ORDER to reduce fossil energy consumption and accelerate global energy transformation, in near future renewable energy integration including wind energy, solar energy, and other clean energy will be the basic form of new-type power systems, which are characterized by high penetrations of both renewables and power electronics devices [1], [2]. In recent years, a large number of renewable equipment, such as permanent magnet synchronous generator (PMSG), doubly fed induction generator, photovoltaic, etc. are connected to the grids through power electronic converters [3]. Different from synchronous generator (SG), the synchronization between renewable equipment is realized by controllers, with a weak overcurrent capacity. To make renewable equipment not easily off-grid after large disturbances, grid-connected guidelines require that renewable equipment has the ability of low voltage ride through (LVRT) [4]. Therefore, after severe faults, renewable equipment should automatically switch to the transient control scheme and trigger some hardware protections. Clearly, these make the transient process of the new-type power systems much more complicated and their transient stability mechanism remains to be studied [5], [6].

With the rapid development of wind power generation technology, the PMSG has gradually become a mainstream generator of wind turbines [7]. At the same time, the transient synchronous stability of the PMSG grid-connected system has become a research hotspot in recent years [8], [9]. Early researches have mainly studied the influence of PMSG on the SG by simulations [10], [11], [12] and usually depended on specific system topology and engineering scenario. Based on the fast control characteristics of wind turbines, some researchers believed that wind turbines can be approximated as parallel negative resistance and negative reactance [13], constant power source [14], and controlled current source [15], etc. In addition, the power angle curve was analyzed and the equal area criterion (EAC) was used to judge system transient stability.

With increase of renewables, researchers gradually began to pay more attention to the transient stability of PMSG itself. During the LVRT, the PMSG switches to the transient control by triggering transient switching control (TSC), and its transient is actually very complicated. However, in the during-fault stage by ignoring the hardware protection circuit and the AC current control (ACC) dynamics, the PMSG dynamics can be simplified to a phase-locked loop (PLL) dynamics [16], [17], [18], [19], [20]. For this simple second-order system, some classical methods including the Lyapunov stability theorem [21], [22], EAC [23], [24], phase portrait approach [25], etc. have been developed. The influence of converter capacity and PLL output frequency limitations on the transient stability of the PLL system has been studied very recently [26], [27], [28]. In addition, it is found that for the PMSG grid-connected system with the addition inertia control (AIC), the electromechanical timescale dynamics of the machine-side converter (MSC) can greatly affect the PLL dynamics, which in turn affects the transient stability of the system [29]. For two recent studies mainly focusing on the switching effect of the voltage source converter (VSC) grid-connected system under the LVRT [30], [31], the switching control characteristics was studied by transforming all state-dependent switching conditions into time-dependent ones [30], and the different transient-stage models were established [31]. In [31], each transient-stage model was still simplified into a second-order PLL model with similar forms, and then analyzed by the EAC in a unified manner. However, more complicated problem of transient stability of the PMSG grid-connected system with the TSC has not been investigated so far, to the best knowledge of the authors.

On the other hand, mainly for the goal of electromagnetic transient simulations, several wind turbine manufacturers have established the PMSG models according to their respective transient control schemes [32]. A universal model of the PMSG considering the TSC was constructed by General Electric and the Western Electricity Coordinating Council in the United States [33], [34]. In [35], the effects of different LVRT control schemes, different active power climbing rates, and PLL bandwidth on the PMSG transient characteristics were analyzed relying on these detailed models. However, clearly these models and some associated studies are mainly for time-domain electromagnetic transient simulations and not directly for mechanism analysis.

Consequently, this article aims to establish a clear physical picture for the entire transient process of the PMSG grid-connected system by considering TSC under severe faults, analyze the impact of major parameters, and reveal transient synchronous stability mechanism. The main contributions are as follows.

1) The entire transient process of the PMSG grid-connected system can be divided into four stages: prefault (stage 1), during-fault (stage 2), early postfault (stage 3), and late postfault (stage 4). For each stage, the corresponding simplified mechanism models are established and the machine–network interface relations are uncovered.
2) The main parameters of each stage are analyzed. For stage 2, the values of the infinite-bus voltage dip and the active-power current output are dominant. For stage 3, it is found that the variation of the active current climbing rate does not change the system stability. For stage 4, a method is proposed to judge the system stability by projecting high-dimensional system stable region on the PLL phase-frequency 2-D plane. The size of the system stable region is positively correlated with the recovered infinite-bus voltage.
3) For the system transient stability after the whole four stages, stage 2 can be either stable or unstable under the condition that the fault is cleared before the critical clearing time (CCT), i.e., the loss of synchronization in stage 2 does not mean the system instability. Therefore, the transient stability on the during-fault stage is only a sufficient condition, but not a necessary condition, and actually the system can be stable under wider parameter

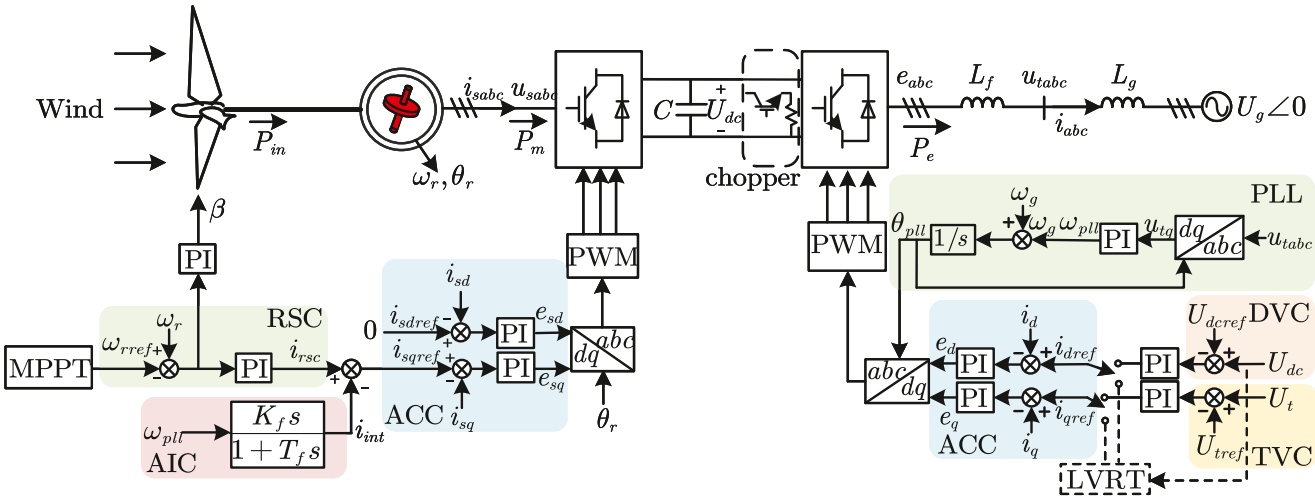

Fig. 1. Schematic show of the single-PMSG infinite-bus system.

regions. This is fundamentally different from most of previous studies on this problem.

The rest of this article is orgnized as follows. In Section II, the topology and the TSC scheme of the PMSG grid-connected system are introduced and the entire transient process is divided into four stages. In Section III, the simplified models for each stage are established and their machine–network interface relationships are obtained. In Section IV, the transient synchronous characteristics are analyzed in each stage, and the transient stability mechanism is uncovered. The experimental verification is given in Section V. Finally, conclusions and discussions are presented in Sections VI and VII, respectively.

II. Single-PMSG Infinite-Bus System and Transient Stage Decomposition

Fig. 1 shows the topology structure of the single-PMSG infinite-bus system. For the MSC), it adopts the zero d-axis current control, including the maximum power point tracking, pitch control, rotor speed control (RSC), AIC, and ACC. Since the pitch control and the maximum power point tracking basically do not operate during the transient process, they are ignored in the article. The q-axis current reference of the stator i_{sqref} is given by both the RSC and AIC, and the d-axis current reference of the stator i_{sdref} is set to zero. The ACC generates the internal potentials e_{sd} and e_{sq} based on the current references. After the coordinate transformation, the trigger signals are generated by the pulsewidth modulation.

The MSC is connected to the grid-side converter (GSC) by a dc capacitor C, and the GSC is connected to the infinite-bus by a filter inductance L_f and a line inductance L_g. For the GSC, it consists of the dc-link voltage control (DVC), terminal voltage control (TVC), ACC, and PLL. The DVC and TVC give the d-axis and q-axis current references, i_{dref} and i_{qref}, by controlling the capacitor voltage U_{dc} and the terminal voltage U_t, respectively. Similarly, the ACC generates the internal potentials e_d and e_q based on the current references, and the trigger signals are generated by the pulsewidth modulation.

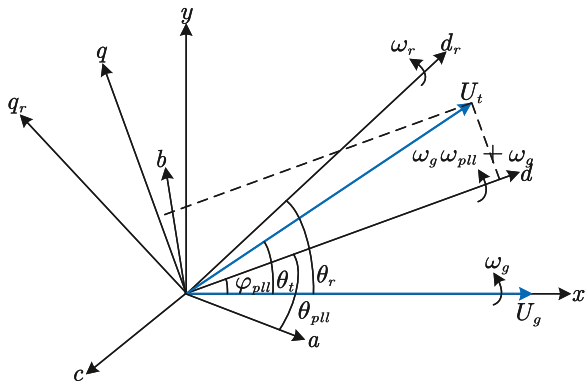

Fig. 2. Schematic shows of the three-phase stationary abc, the dq reference frames of MSC and GSC, and the xy common reference frame, accompanying with several major angles used in the article.

The PLL provides a phase basis for the angle transformation between the dq reference frame of the GSC and the abc reference frame. To be clear, Fig. 2 shows the relationship between the dq reference frame of the MSC and GSC and the xy common reference frame, associated with several major angles used in the article.

According to the wind turbine grid-connected guidelines in China [4], when the positive sequence component of the PMSG point-of-common-coupling voltage is lower than 80% of the nominal voltage, the TSC needs to be switched on. Since this article focuses on the PMSG external characteristics, all the TSCs within the ACC (about 10 ms) and the electromechanical (about 1 s) timescales are neglected and only controllers within the DVC (about 100 ms) timescale are considered. For the hardware protection devices, this article only considers the chopper and meanwhile ignores its overheating limit, that is, the chopper is allowed to continuously switch ON and OFFduring the transient process. Therefore, the whole transient process can be divided into four different stages: prefault (stage 1), during-fault (stage 2), early postfault (stage 3), and late postfault (stage 4). In particular, 1) in the prefault stage 1, it is always assumed as

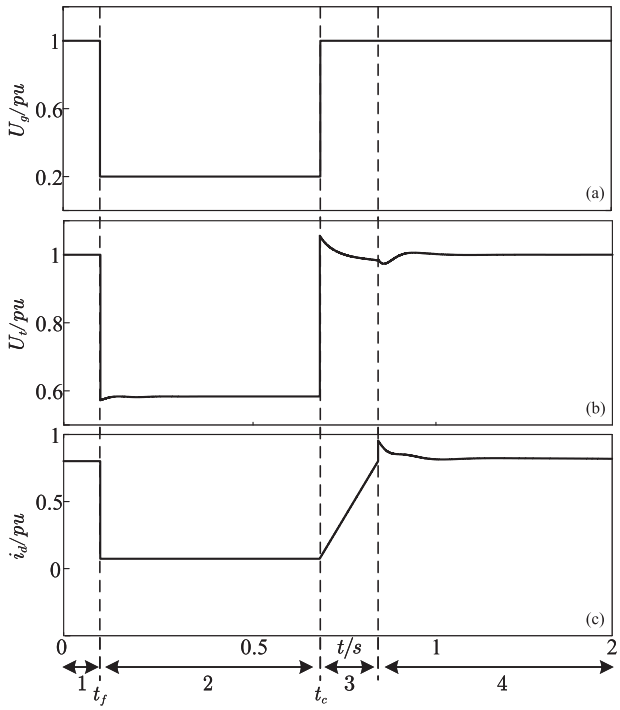

Fig. 3. Schematic shows of four transient stages including pre-fault (stage 1), during-fault (stage 2), early post-fault (stage 3), and late post-fault (stage 4), accompanying with some typical trajectories of U_g, U_t, and i_d. Here, t_f denotes the fault occurrence time and t_c the fault clearing time.

stable. 2) In the during-fault stage 2, after a certain fault for the terminal voltage U_t being lower than its 80% nominal voltage, the DVC and TVC are disconnected, and the current references is switched to the transient control to provide voltage support. At the same time, with the increase of U_{dc}, the chopper performs short-circuit discharge on the dc capacitor, to prevent U_{dc} from rising too high. 3) In the early postfault stage 3, the infinite-bus voltage is restored and the fault is cleared. Meanwhile, the reactive-power and active-power current branches are switched to the TVC and the climbing control, respectively. 4) In the late postfault stage 4, as the active current reaches the reference, the DVC is switched ON and the whole system is gradually restored.

The whole transient process by the time-domain trajectories of the infinite-bus voltage U_g, terminal voltage U_t, and active-power current output i_d is shown in Fig. 3. Here, t_f denotes the fault occurrence time and t_c is the fault clearing time. Only their difference $t_c - t_f$ for the fault duration time is meaningful. In addition, the CCT is used to represent the CCT. Namely, only under $t_c - t_f <$ CCT, the system is transient stable. Afterward, subscripts 1, 2, 3, and 4 for the corresponding stages will always be used.

III. Nonlinear Modeling of PMSG Considering TSC Under Severe Faults

A. Stage 1: Prefault

The PMSG adopts the conventional controls in stage 1. For the mechanism study, it is necessary to simplify the model while capturing its dominant behaviors. Due to the multiscale cascade control of the PMSG, the dynamics of the RSC and AIC belong to the electromechanical timescale, whose frequency bandwidth is about a few hertz. The dynamics of the DVC and TVC belong to the dc voltage timescale, whose bandwidth is about dozens of hertz. Meanwhile, the dynamics of ACC is within the ac current timescale, whose bandwidth is about hundreds of hertz. At the same time, due to the AIC, the electromechanical timescale dynamics of the MSC can affect the PLL dynamics, which changes it from electromagnetic to electromechanical timescale [29]. Since the system transient behavior is dominated by the slow timescale, we can ignore the controls of fast timescale and retain those of slow timescale. Therefore, in this stage, we ignore the DVC, TVC, and ACC, and consider the rotor dynamics, RSC, AIC, and PLL.

The differential equations for the rotor, RSC, and AIC are

$$2H\dot{\omega}_{r1} = P_{in} - P_{m1} \tag{1}$$

$$\dot{i}_{sq1} = k_{p,\text{rsc}}\dot{\omega}_{r1} + k_{i,\text{rsc}}\left(\omega_{r1} - \omega_{\text{rref}}\right) - \dot{i}_{\text{int1}} \tag{2}$$

$$T_f\dot{i}_{\text{int1}} = -i_{\text{int1}} + K_f\dot{\omega}_{\text{pll1}} \tag{3}$$

where ω_{r1} is the frequency of rotor, i_{sq1} is the q-axis current of MSC, i_{int1} is the output current of AIC, and ω_{pll1} is the output frequency of PLL. H represents the inertial constant of the rotor, P_{in} denotes the input mechanical power of the PMSG, P_{m1} is the output electromagnetic power of the MSC, and ω_{rref} is the frequency reference of rotor. $k_{p,\text{rsc}}$ and $k_{i,\text{rsc}}$ are the proportional and integral (PI) parameters of RSC, respectively. Since the MPPT and the pitch control are ignored, P_{in} is constant.

The differential and algebraic equations for the PLL, respectively, are

$$\begin{cases}\dot{\varphi}_{\text{pll1}} = \omega_g\omega_{\text{pll1}} \\ \dot{\omega}_{pll1} = k_{p,\text{pll}}\dot{u}_{tq1} + k_{i,\text{pll}}u_{tq1}\end{cases} \tag{4}$$

and

$$u_{tq1} = U_{t1}\sin\left(\theta_{t1} - \varphi_{\text{pll1}}\right) \tag{5}$$

where φ_{pll1} is the output phase of PLL, ω_g is the rotation frequency of the xy common reference frame, u_{tq1} is the terminal voltage in the q-coordinates, and $k_{p,\text{pll}}$ and $k_{i,\text{pll}}$ are the PI parameters of the PLL. U_{t1} is the terminal voltage of the GSC at stage 1 and θ_{t1} is the terminal phase of the GSC. Since the TVC is fast and can be ignored, $U_{t1} = U_{\text{tref}}$, where U_{tref} denotes the reference of the terminal voltage.

Due to the zero d-axis current control (i.e., $i_{sd1} = 0$), we have

$$\begin{aligned}P_{m1} &= \omega_{r1}T_{m1} = \omega_{r1}\left[i_{sq1}\psi_r - \left(L_d - L_q\right)i_{sd1}i_{sq1}\right] \\ &= \omega_{r1}i_{sq1}\psi_{r1}\end{aligned} \tag{6}$$

where ψ_r represents the (constant) rotor flux of the PMSG, T_m is the electromagnetic torque of the PMSG, and L_d and L_q are the d-axis and q-axis stator inductances of the PMSG, respectively.

As the electromagnetic timescale controls are neglected, $P_{m1} = P_{e1}$. Therefore, P_{e1} can written as

$$P_{e1} = \frac{U_{t1}U_{g1}}{X_g}\sin\theta_{t1} \tag{7}$$

or

$$\theta_{t1} = \arcsin \frac{P_{e1} X_g}{U_{t1} U_{g1}} = \arcsin \frac{P_{m1} X_g}{U_{t1} U_{g1}} \tag{8}$$

where $X_g = \omega_g L_g$.

As a result, taking $\mathbf{X} = [\omega_{r1}, i_{sq1}, i_{\text{int}1}, \varphi_{pll1}, \omega_{pll1}]^{\text{T}}$ as the state variables and combining the above equations from (1) to (8), the corresponding differential-algebraic equations (DAEs) for the PMSG grid-connected system at stage 1 are

$$\begin{cases} 2H\dot{\omega}_{r1} = P_{in} - P_{m1} \\ \dot{i}_{sq1} = k_{p,\text{rsc}}\dot{\omega}_{r1} + k_{i,\text{rsc}}\left(\omega_{r1} - \omega_{\text{rref}}\right) - \dot{i}_{\text{int}1} \\ T_f \dot{i}_{\text{int}1} = -i_{\text{int}1} + K_f \dot{\omega}_{\text{pll}1} \\ \dot{\varphi}_{pll1} = \omega_g \omega_{\text{pll}1} \\ \dot{\omega}_{pll1} = k_{p,\text{pll}}\dot{u}_{tq1} + k_{i,\text{pll}} u_{tq1} \end{cases} \tag{9}$$

$$\begin{cases} P_{m1} = \omega_{r1} i_{sq1} \psi_r \\ u_{tq1} = U_{t1} \sin\left(\theta_{t1} - \varphi_{\text{pll}1}\right) \\ U_{t1} = U_{\text{tref}} \\ \theta_{t1} = \arcsin \frac{P_{m1} X_g}{U_{\text{tref}} U_{g1}} \end{cases}. \tag{10}$$

It can be seen that it is a five-dimensional nonlinear system with the nonlinear terms: $\omega_{r1} i_{sq1} \psi_r$, $U_{\text{tref}} \sin(\theta_{t1} - \varphi_{pll1})$, and $\arcsin(P_{m1} X_g / U_{\text{tref}} / U_{g1})$. It is notable that to keep a simple structure, they have not been expressed as the usual explicit state-variable equations. This manipulation will be used for other stages. In addition, as stage 1 is always assumed as stable, it provides initial conditions for the following stages.

In our recent work [29], the above DAEs for the PMSG grid-connected system at stage 1 has been studied within the framework of shallow fault, namely, the fault destroy degree is still tiny and the following switching controls in the LVRT is not triggered. In contrast, all transient processes by considering switching dynamics within the framework of severe faults will be studied in this article.

B. Stage 2: During-Fault

In the stage 2, for a terminal voltage dip, the PMSG switches to the TSC. Although the MSC and the GSC are coupled due to the AIC, the capacitor voltage U_{dc} is limited to a certain range (1.05–1.15 p.u.) due to the chopper [36], [37]. At the same time, the DVC and TVC are disconnected, and the d-axis and q-axis current references are directly given. Therefore, the MSC is essentially decoupled from the GSC. Further ignoring the ACC dynamics, the PLL dynamics is dominant. The control target of stage 2 is to provide grid voltage support and output sufficient reactive power. According to the current injection method in [4], the d-axis and q-axis current references at stage 2 are

$$\begin{cases} i_{q2} = K\left(U_{t2} - 0.9\right) + i_{q1} \\ 0 \le i_{d2} \le i_{d2\_\max} = \sqrt{I_N^2 - i_{q2}^2} \end{cases} \tag{11}$$

where K represents the reactive current ratio coefficient and I_N is the rated current ($I_N = 1.1$ p.u. is usually chosen). Here, i_{q1} denotes the q-axis current in stage 1, and i_{q2} the q-axis current in stage 2. In engineering, $1.5 < K < 3$ is often chosen.

Based on the network relationships, the dq-axis terminal voltage of the PMSG can be expressed as

$$\begin{cases} u_{tq2} = -U_{g2} \sin \varphi_{\text{pll}2} + X_g i_{d2} \\ u_{td2} = U_{g2} \cos \varphi_{\text{pll}2} - X_g i_{q2} \\ U_{t2} = \sqrt{u_{td2}^2 + u_{tq2}^2} \end{cases} \tag{12}$$

where u_{td2} and u_{tq2} are the d-axis and q-axis terminal voltages, respectively. The infinite-bus voltage dip from U_{g1} to U_{g2} will inevitably produce the dip of U_{t2} and trigger the TSC. Then, stage 2 starts.

As a result, combining (4), (11), and (12), the DAEs in stage 2 are simple, expressed as

$$\begin{cases} \dot{\varphi}_{\text{pll}2} = \omega_g \omega_{\text{pll}2} \\ \dot{\omega}_{pll2} = k_{p,\text{pll}}\dot{u}_{tq2} + k_{i,\text{pll}} u_{tq2} \end{cases} \tag{13}$$

$$\begin{cases} u_{tq2} = -U_{g2} \sin \varphi_{\text{pll}2} + X_g i_{d2} \\ u_{td2} = U_{g2} \cos \varphi_{\text{pll}2} - X_g i_{q2} \\ U_{t2} = \sqrt{u_{td2}^2 + u_{tq2}^2} \\ i_{q2} = K\left(U_{t2} - 0.9\right) + i_{q1} \\ 0 \le i_{d2} \le i_{d2\_\max} = \sqrt{I_N^2 - i_{q2}^2} \end{cases}. \tag{14}$$

In the whole stage 2, although i_{q2} is determined by U_{t2}, as U_{t2} is nearly unchanged, i_{q2} is often chosen as fixed. Here, the value of U_{t2} in the fourth equation in (14) is chosen and fixed as that at the beginning of stage 2. Meanwhile, i_{d2} is also chosen as a fixed adjustable parameter in the whole stage 2, except that it is limited by the total current I_N based on the last inequality in (14). In the next section, we will mainly study the impact of i_{d2}. In this respect, the PLL second-order dynamics (13) with the constant values of i_{d2} and i_{q2} is dominant in this stage, and it has been widely studied [21], [22], [23], [24], [25], [26]. At the same time, the other variables ω_r, i_{sq}, and i_{int} [in (9)] are unidirectionally driven by the PLL dynamics of φ_{pll} and ω_{pll}.

C. Stage 3: Early Postfault

In stage 3, after the fault is cleared, the terminal voltage U_t is restored. As the chopper still works, the PMSG dynamics is dominated by the GSC. The reactive-power and active-power branches switch to the TVC and the active current climbing control, respectively. At this time, the major controls are the TVC, PLL, and active current climbing control. Correspondingly, the differential equations for the active current climbing control and the TVC are

$$\dot{i}_{d3} = k_{\text{ramp}} \tag{15}$$

$$\dot{i}_{q3} = k_{p,\text{tvc}}\dot{U}_{t3} + k_{i,\text{tvc}}\left(U_{t3} - U_{\text{tref}}\right) \tag{16}$$

where k_{ramp} is the active current climbing rate, and $k_{p,\text{tvc}}$ and $k_{i,\text{tvc}}$ are the PI parameters of the TVC. In engineering practice, k_{ramp} is often limited; $5 \le k_{\text{ramp}} \le 15$.

TABLE I
PARAMETER SETTING IN THE PMSG GRID-CONNECTED SYSTEM

Category	Symbol	Numerical Value
Rated Parameter	S_b	2 MVA
	U_b	$690\sqrt{2}$ V
	ω_g	100π
Circuit Parameter	P_{in}	0.8 p.u.
	L_g	$0.5/\omega_g$ H
	U_g	1.0 p.u.
	H	4 p.u.
	ψ_r	0.9 p.u.
	I_N	1.1 p.u.
Controller Parameter	$k_{p,rsc}/k_{i,rsc}$	10/40
	K_f/T_f	10/1
	$k_{p,pll}/k_{i,pll}$	50/2000
	$k_{p,tvc}/k_{i,tvc}$	1/100
	U_{tref}	1.0
	ω_{rref}	1.0
	K	2
	i_{d2}	0.1
	k_{ramp}	5

Finally, combining (4), (12), (15), and (16), the DAEs in stage 3 are

$$\begin{cases} \dot{i}_{d3} = k_{\text{ramp}} \\ \dot{i}_{q3} = k_{p,\text{tvc}}\dot{U}_{t3} + k_{i,\text{tvc}}\left(U_{t3} - U_{\text{tref}}\right) \\ \dot{\varphi}_{pll3} = \omega_g\omega_{\text{pll3}} \\ \dot{\omega}_{\text{pll3}} = k_{p,\text{pll}}\dot{u}_{tq3} + k_{i,\text{pll}}u_{tq3} \end{cases} \tag{17}$$

$$\begin{cases} u_{tq3} = -U_{g3}\sin\varphi_{pll3} + X_g i_{d3} \\ u_{td3} = U_{g3}\cos\varphi_{pll3} - X_g i_{q3} \\ U_{t3} = \sqrt{u_{td3}^2 + u_{tq3}^2} \end{cases}. \tag{18}$$

D. Stage 4: Late Postfault

Under the condition that the active current i_{d4} reaches the reference at stage 1, i_{d1}, the PMSG switches back to the conventional control, and the stage 4 starts. As in the steady state, $P_{\text{in}} = P_{m1} = P_{e1} = u_{td1}i_{d1} + u_{tq1}i_{q1}$, $u_{td1} = U_{\text{tref}} = 1$ p.u., and $u_{tq1} = 0$, then $P_{\text{in}} = i_{d1}$ can be obtained. In the article, $P_{in} = i_{d1} = 0.8$ p.u. is chosen, as shown in Table I. Therefore, the switching condition for stage 4 becomes $i_{d4} = 0.8$ p.u. Except this, the DAEs in stage 4 are the same as those in stage 1. In particular, the subscripts should change from 1 to 4, which indicate values in the stage 4.

E. Machine–Network Interface

On the basis of the above simplified model in each stage, the machine–network interface relations between the PMSG and the network are also clear. The results are summarized in Fig. 4. For details, Fig. 4(a) shows the machine–network interface in stage 1, where $\dot{\mathbf{x}}_\mathbf{1} = \mathbf{f_1}(\mathbf{x_1}, z)$ is given in (9), $z = h(\varphi_{pll1}, \theta_{t1})$ (here $z = u_{tq1}$) in (5), and $P_{m1} = g(\mathbf{x_1})$ in (6). Specifically, the PMSG outputs the electromagnetic power P_m and the terminal voltage amplitude U_t to the network, and the network outputs the voltage angle θ_t to the PMSG. Fig. 4(b) shows the machine–network interface in stage 2, where $\dot{\mathbf{x}}_\mathbf{2} = \mathbf{f_2}(\mathbf{x_2}, \mathbf{y})$ is shown in (13), $\mathbf{I} = v(\mathbf{y})$ is in (14), and $\mathbf{y}$ represents the algebraic variable. In particular, the PMSG outputs the d-axis and q-axis currents, i_d and i_q, to the network, and the network outputs the d-axis and q-axis voltages, u_{td} and u_{tq}, to the PMSG. Similarly Fig. 4(c) shows the machine–network interface in stage 3, where $\dot{\mathbf{x}}_\mathbf{3} = \mathbf{f_3}(\mathbf{x_3}, \mathbf{y})$ in (17). Finally, Fig. 4(d) shows that in stage 4, which is the same as in stage 1.

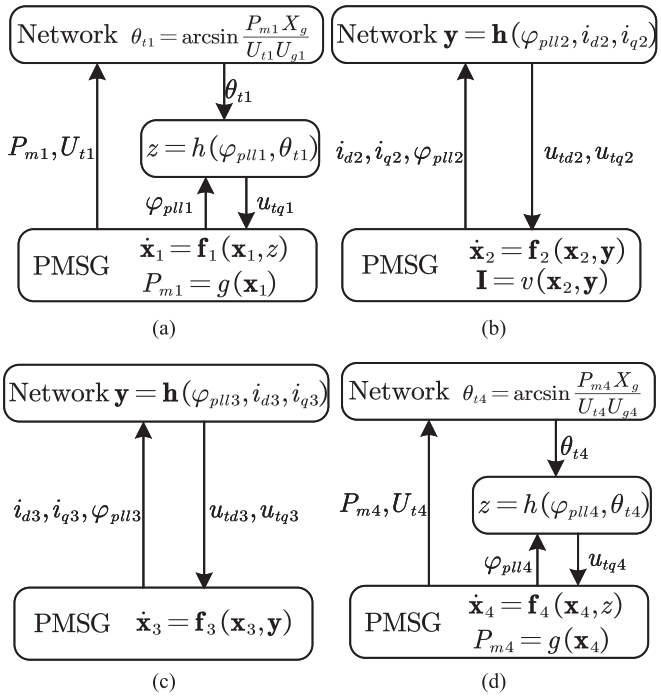

Fig. 4. Schematic shows of machine-network interface in each stage. (a)–(d) correspond to stages 1–4, respectively.

As a result, at stages 1 and 4, the electromechanical timescale dynamics of the machine-side rotor is dominant, whereas at stages 2 and 3, the electromagnetic timescale dynamics of the GSC is dominant. Obviously Fig. 4 establishes a simple physical picture for how the PMSG works and how it interacts with the grid at different LVRT stages. To be compared with the two recent works on the VSC system considering the switching control [30], [31], clearly it catches the dominant elements in the whole transient process, although it looks more complicated.

F. Simulation Verification

In order to verify the above analysis, the simplified models and the detailed electromagnetic model of the PMSG grid-connected system with the TSC in Fig. 1 are built and compared in MATLAB/Simulink. The results are shown in Fig. 5. At $t_f = 0.1$ s, the infinite-bus voltage U_g dips to 0.2 p.u., and at $t_c = 0.7$ s, the fault is cleared and U_g recovers to 1 p.u. For the fault duration

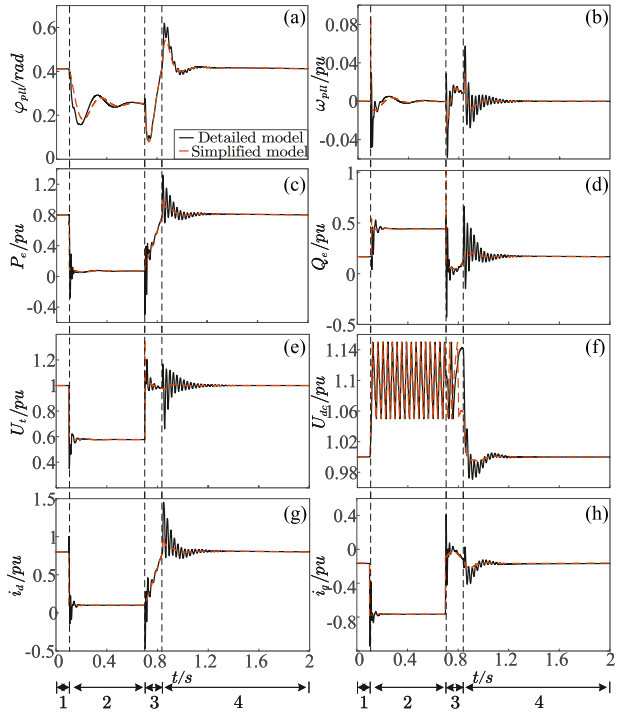

Fig. 5. (a)–(h) Simulation comparisons of the simplified and detailed models after faults for φ_{pll}, ω_{pll}, P_e, Q_e, U_t, U_{dc}, i_d, and i_q, respectively.

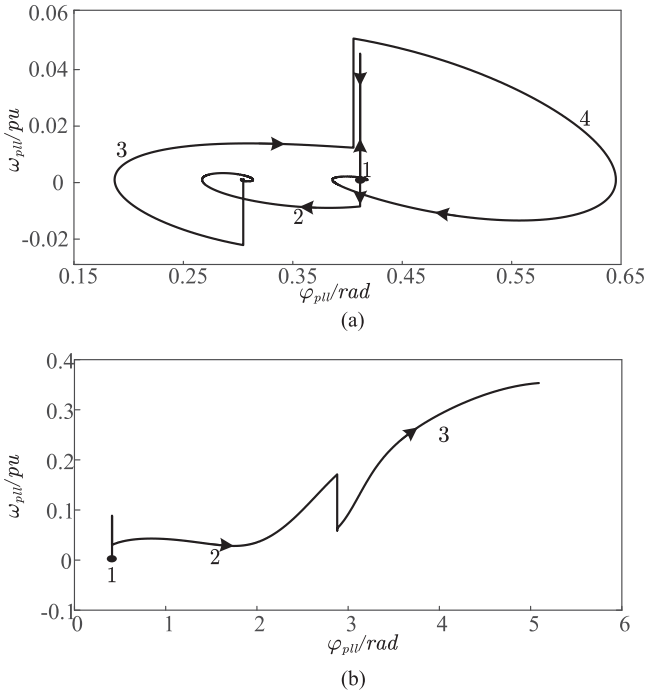

Fig. 6. Plots of transient response trajectories after faults. (a) $i_{d2} = 0.1$ p.u. and $t_c = 0.7$s, (b) $i_{d2} = 0.38$ p.u. and $t_c = 0.37$s.

time, $t_c - t_f = 0.6$ s. To be clear, Table I shows the parameters in simulations.

Generally, the short-circuit ratio (SCR) has been employed to characterize the grid strength, which can be expressed as $\text{SCR} \approx 1/X_g$ [38]. Under the parameter $X_g = 0.5$ p.u. in this article, the SCR is 2, which belongs to an extremely weak network ($\text{SCR} \leq 2$). In the Appendix, we also validate the above model under $\text{SCR} = 3$ and 5. The corresponding additional comparison results are shown in Figs. 25 and 26, respectively.

In all these figures, it can be seen that they fit well in all transient stages, except some high-frequency oscillations, and these high-frequency oscillations weaken as the grid strength increases, as shown in Figs. 25 and 26. Meanwhile, the transient switches are clear. For example, in stage 1, the PMSG adopts the conventional control, and the simplified model (9) and (10) provides the initial operating point. After the faults, the DVC and TVC are disconnected and the transient control scheme is switched ON in stage 2. The q-axis current i_{q2} is obtained and fixed according to (11). The d-axis current i_{d2} is chosen as an adjustable parameter, limited by (11). The chopper begins to continuously operate to consume the surplus active power output by the MSC, and the MSC and the GSC are decoupled. When the fault is cleared, the system transits to stage 3. The reactive power branch is reswitched to the TVC, and the active power branch is switched to the climbing control. At this time, the MSC and the GSC are still decoupled. After a while, when the active current equals to the current reference of stage 1 (i.e., $i_{d4} = i_{d1} = 0.8$ p.u.), the active power branch switches to the DVC immediately, and the chopper quits. Therefore, the system transits to stage 4, and the MSC and the GSC are recoupled.

To be clearer, Fig. 6(a) and (b) shows the typical stable and unstable trajectories on the φ_{pll}-ω_{pll} phase plane, respectively. The black dot denotes the equilibrium point in stages 1 and 4, and numbers 1–4 represent the corresponding stages. The system is stable after all four stages in Fig. 6(a), whereas it is unstable and goes to infinity in Fig. 6(b). It can also be found that at the moment of each control switching, the ω_{pll} is discontinuous due to the impact of algebraic loop [39], while φ_{pll} is always continuous.

IV. Transient Stability Characteristics Analysis

Although the TSC makes the transient dynamics of the PMSG much more complex, the fundamental condition for transient stability might be unchanged, that is, whether the system state is within the stable region at the beginning of stage 4. In the transient process, stage 1 provides the initial operating point, the fault trajectory continuously changes in stages 2 and 3, and the stable region is determined by the stable operating point (or called equilibrium point) of stage 4. Therefore, similar to the transient stability in the traditional power system [40], here it is still determined by two separate conditions: stable region of the final stage 4 and fault-on trajectory after all middle stages 2 and 3. In the following, for the transient stability characteristic analysis, this article will concentrate on these two aspects.

A. Stage 1 and 4: Prefault and Late Postfault

As we know, stage 1 simply provides an initial operating point, whereas stage 4 provides the system stable region. Since

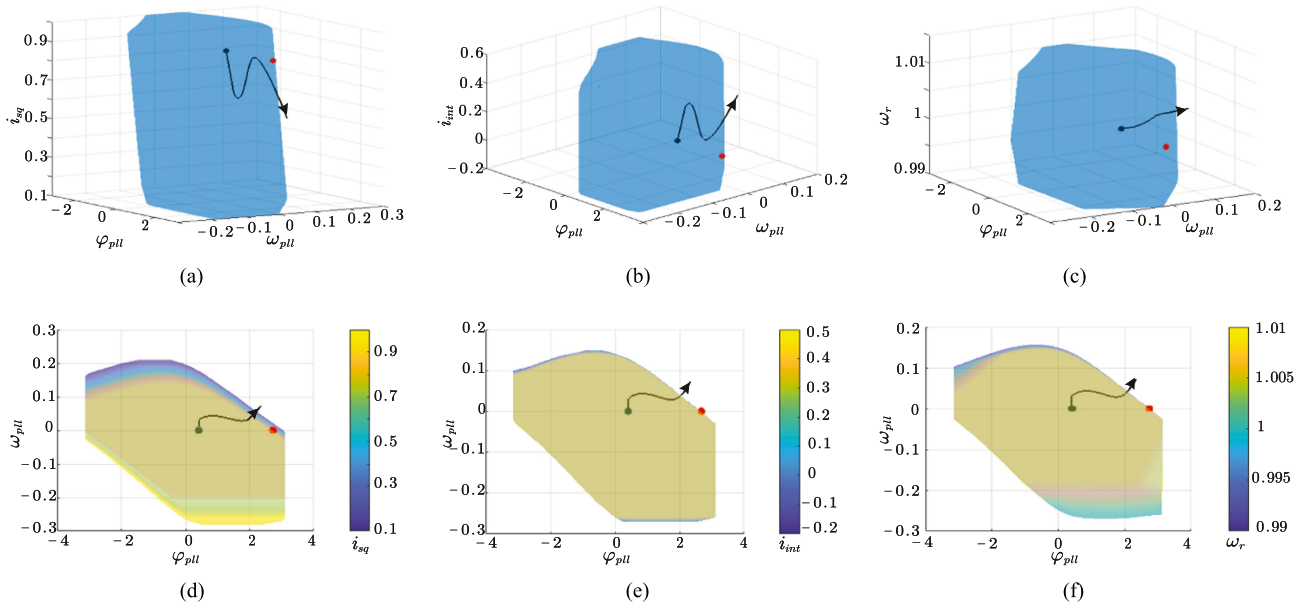

Fig. 7. Illustrations of stable regions in (a) φ_{pll}-ω_{pll}-i_{sq}, (b) φ_{pll}-ω_{pll}-i_{int}, and (c) φ_{pll}-ω_{pll}-ω_r 3-D spaces, respectively. (d), (e), and (f) are the projections on the φ_{pll}-ω_{pll} phase plane of (a), (b), and (c), respectively. The black curve represents the instability trajectory. The black and red dots denote the stable and UEPs in stage 4, respectively.

the simplified model in stage 4 is a five-dimensional nonlinear system, its stable region cannot be easily depicted. Therefore, in Fig. 7(a), (b), and (c), it is projected into the φ_{pll}-ω_{pll}-i_{sq}, φ_{pll}-ω_{pll}-i_{int}, and φ_{pll}-ω_{pll}-ω_r 3-D spaces, respectively. The other variables ω_r, i_{sq}, and i_{int} are fixed as the steady-state values of the unstable equilibrium point (UEP), i.e., $\omega_r = 1$, $i_{\text{sq}} = 0.89$, and $i_{\text{int}} = 0$. The black curve represents a fault-on trajectory. The black and red dots are for the stable equilibrium point and UEP, respectively. In all these three sub-figures, the φ_{pll}-ω_{pll} is always used as the bottom surface $x - y$ of the stable region. It is clear that the stable region always shows a cylinder regardless of which z-axis state variable is used. In addition, Fig. 7(d), (e), and (f) represents their projections of Fig. 7(a), (b), and (c) directly onto the φ_{pll}-ω_{pll} phase plane, respectively. The lighter the color, the larger the z-axis variable. They obviously show that the unstable trajectory always passes through the stable region near the UEP, and the basin boundary near the UEP hardly changes with the change of the z-axis variable. Thus, the stability can be well determined by the two dominant variables, φ_{pll} and ω_{pll}. This finding is also supported by our recent observation that the φ_{pll} is the dominant instability variable of the VSC grid-connected system, similar to the rotor angle in the SG [41], [42].

Therefore, to simplify analysis, it is reasonable to judge system stability by projecting the original five-dimensional stable region on the PLL phase-frequency 2-D plane to determine its transient stability. Fig. 8 shows the influence of U_{g4} in stage 4 on the size of the system stable region. Similarly the other variables ω_r, i_{sq}, and i_{int} are fixed as the steady-state values of the UEP, i.e., $\omega_r = 1$, $i_{\text{sq}} = 0.89$, and $i_{\text{int}} = 0$. Clearly, the size of the stable region is positively correlated with U_{g4}, which is consistent with our common sense.

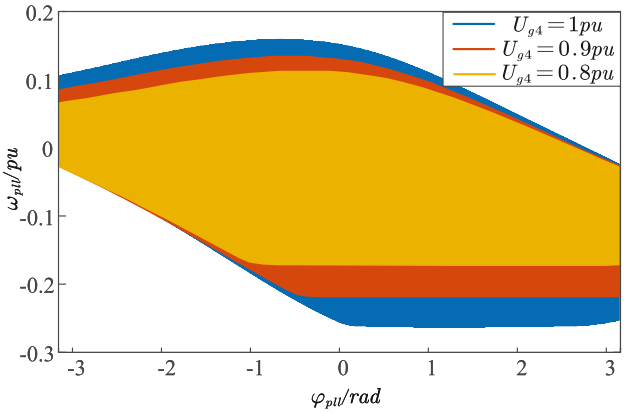

Fig. 8. Plots of stable region on the φ_{pll}-ω_{pll} plane for different U_{g4}'s, with all other variables ω_r, i_{sq}, and i_{int} fixed as the steady-state values of the UEP.

B. Stage 2: During-Fault

Clearly both stages 2 and 3 determine the fault trajectory. As we will see, stage 3 does not play an active role in the transient stability. In this section, let us focus on stage 2.

Usually for the transient stability in the traditional power systems, there is no any concept of operation point and transient stability in the during-fault stage, as the during-fault state is only a nonstationary state connecting the prefault and postfault states [40]. However, the during-fault stage stability in the new-type power systems has been widely studied. Based on the model analysis in Section III, the model in stage 2 is an autonomous system in mathematics and it can also have its own equilibrium point. Therefore, if the system is stable in stage 2, it can quickly settle down to an operating point after a certain

transient time and it is also easy to sustain stability through stage 3 afterward. In addition, the transient time of stage 2 should not exceed 625 ms, which is required by the grid codes [4]. On the other hand, other possibility also exists. Namely, if the system is unstable in stage 2, under the conditions that the fault is cleared in time and before the CCT, the system can still be stable by the subsequent climbing control. Therefore, these two different possibilities should be separately studied.

1) System is Stable in Stage 2: Substituting the first equation in (14) into (13), the simplified model in stage 2 can be written as

$$M\ddot{\varphi}_{\text{pll2}} = P'_m - P'_e + D\dot{\varphi}_{\text{pll2}} \tag{19}$$

where

$$\begin{cases} M = \frac{1}{k_{i,\text{pll}}} \\ P'_m = i_{d2}X_g \\ P'_e = U_{g2}\sin\varphi_{\text{pll2}} \\ D = -\frac{k_{p,\text{pll}}}{k_{i,\text{pll}}}U_{g2}\cos\varphi_{\text{pll2}} \end{cases} \tag{20}$$

It can be found that (19) is very similar to the classical SG second-order swing equation. Here, M, P'_m, P'_e, and D in (20) can be regarded as (equivalent) virtual inertia, mechanical power, electromagnetic power, and damping, respectively. At the same time, as i_{d2} is an adjustable parameter, which is limited by the total current I_N based on the last inequality in (14), the value of P'_m should be within the constraint of converter capacity. In addition, since the network dynamics is ignored, (19) and (20) are simpler than the usual second-order PLL model [21], [22], [23], [24], [25], [26]. The two parameters U_{g2} and i_{d2} will be mainly studied.

Set the fault as U_{g2} dips to 0.2 p.u. at $t_f = 0.1$ s and the transient control is activated. By ignoring the equivalent damping D ($D = 0$), the classical EAC for an energy conservation system can be used in the transient stability analysis. Fig. 9 shows three different cases for i_{d2} being 0.3 p.u., 0.35 p.u., and 0.42 p.u. Take Fig. 9(a) as an example. The system is located at the stable equilibrium point a before the fault. When U_g dips, the system shifts to point b. Meanwhile, the equivalent mechanical power drops from P'_{m1} to P'_{m2}, and the equivalent electromagnetic power drops from P'_{e1} to P'_{e2}. As $P'_{m2} > P'_{e2}$, the system enters the acceleration process, and ω_{pll} becomes positive and φ_{pll} increases accordingly. The acceleration area is S_{cbd}. When φ_{pll} comes across point d, P'_{m2} becomes less than P'_{e2}, causing the system to slow down. However, due to $\omega_{\text{pll}} > 0$, φ_{pll} continues to increase. Until $\omega_{\text{pll}} < 0$, φ_{pll} begins to decrease. If the system exceeds the UEP (point f), P'_{m2} will be greater than P'_{e2}, and the system will continue to accelerate and ultimately lose stability. On the contrary, the system will be eventually stable. In other words, the maximum deceleration area is S_{def}.

In Fig. 9(a), $i_{d2} = 0.3$ p.u. and the system is stable, as the deceleration area S_{def} is greater than the acceleration area S_{bcd}, i.e., $S_{\text{def}} > S_{\text{bcd}}$. For $i_{d2} = 0.35$ p.u. in Fig. 9(b), $S_{\text{def}} < S_{\text{bcd}}$ and the system is unstable. In addition, for the worse case of $i_{d2} = 0.42$ p.u. in Fig. 9(c), there is no operating point in stage 2, and the system should also be unstable. Therefore, for the large-disturbance stability analysis of the PMSG in stage 2, the following three constraints should be considered:

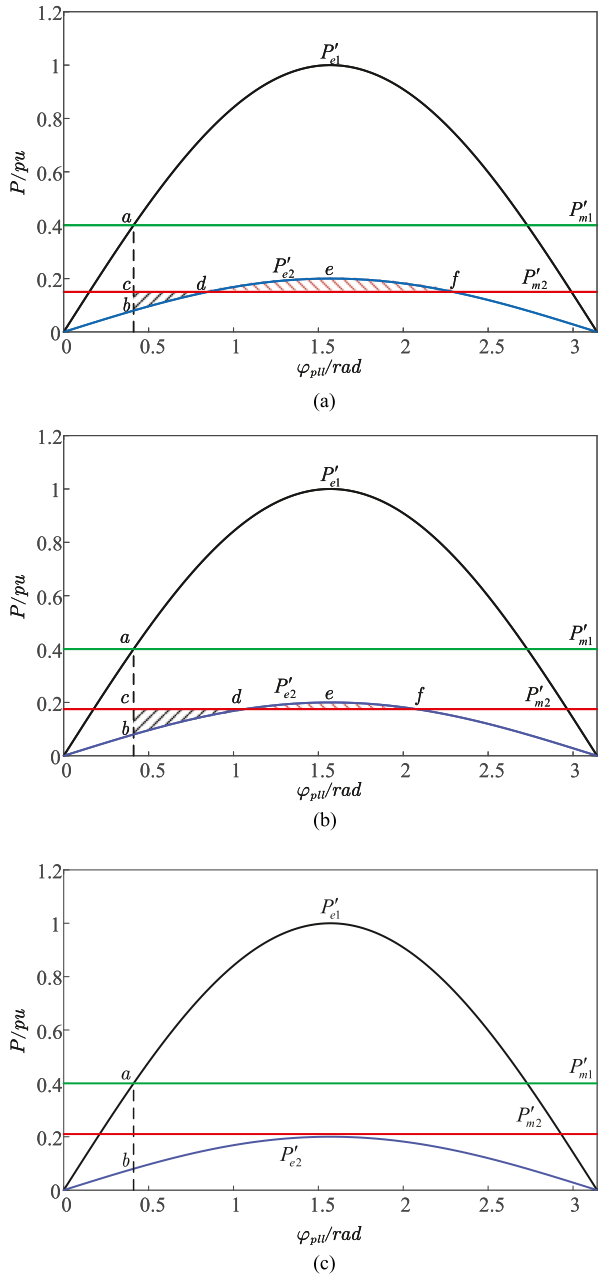

Fig. 9. Schematic shows of transient stability analysis by the EAC. (a) $i_{d2} = 0.3$ p.u., (b) $i_{d2} = 0.35$ p.u., and (c) $i_{d2} = 0.42$ p.u. Operation point does not exist in (c).

Constraint 1: Operating point constraint

In the system, the electromagnetic power P_{e2} can be expressed as

$$P_{e2} = u_{td2}i_{d2} + u_{tq2}i_{q2}. \tag{21}$$

As $u_{tq2} = 0$ and $u_{td2} = U_{t2}$ in the steady state, it immediately yields

$$P_{e2} = U_{t2}i_{d2}. \tag{22}$$

At the same time, due to the power transmission constraint on the network, P_{e2} should be determined by

$$P_{e2} = \frac{U_{t2}U_{g2}}{X_g}\sin\theta_{t2}. \tag{23}$$

Combining (22) and (23), it can be obtained that

$$\theta_{t2} = \arcsin\frac{i_{d2}X_g}{U_{g2}}. \tag{24}$$

Therefore, to ensure that it is solvable, i_{d2} and U_{g2} need to satisfy the following constraint:

$$i_{d2} \le \frac{U_{g2}}{X_g}. \tag{25}$$

Constraint 2: EAC constraint

In order to ensure transient stability, the acceleration area should be smaller than the deceleration area. According to (19) and (20) and ignoring the damping ($D = 0$), this constraint becomes

$$\int_{\varphi_{\text{plla}}}^{\varphi_{\text{plld}}} (P'_m - P'_e)\, d\varphi_{\text{pll}} + \int_{\varphi_{\text{plld}}}^{\varphi_{\text{pllf}}} (P'_m - P'_e)\, d\varphi_{\text{pll}} < 0 \tag{26}$$

where

$$\begin{cases} \varphi_{\text{plla}} = \arcsin\frac{i_{d1}X_g}{U_{g1}} \\ \varphi_{plld} = \arcsin\frac{i_{d2}X_g}{U_{g2}} \\ \varphi_{pllf} = \pi - \arcsin\frac{i_{d2}X_g}{U_{g2}} \end{cases} \tag{27}$$

Here, φ_{plla}, φ_{plld}, and φ_{pllf} represent the angles of points a, d, and f in Fig. 9, respectively.

Therefore, i_{d2} and U_{g2} should be constrained by

$$U_{g2}\left[\cos\left(\pi - \arcsin\frac{i_{d2}X_g}{U_{g2}}\right) - \cos\left(\arcsin\frac{i_{d1}X_g}{U_{g1}}\right)\right] + i_{d2}X_g\left(\pi - \arcsin\frac{i_{d2}X_g}{U_{g2}} - \arcsin\frac{i_{d1}X_g}{U_{g1}}\right) < 0. \tag{28}$$

Constraint 3: Capacity constraint

Due to the limitation of the converter capacity, i_{d2} needs to meet the constraint, as shown the last inequality in (14), where i_{q2} depends on U_{t2} and further U_{g2}.

In summary, the ranges defined by the above three constraints are obtained and shown in Fig. 10, where the green dashed line represents constraint 1, the black double-dot-dashed line represents constraint 2, and the yellow dot-dashed line represents constraint 3. Area I is the range of i_{d2}-U_{g2} under all these constraints. If i_{d2} is chosen within area I, the PMSG should be stable in stage 2, and the CCT is infinite. Clearly for larger U_{g2} and i_{d2}, the capacity constraint is dominant, as shown the upper-right part of area I, whereas for smaller U_{g2} and i_{d2} (for a severe fault dip), as shown the lower-left part of area I, the EAC constraint plays a leading role.

2) System is Unstable in Stage 2: So far, the transient stability in the single stage 2 has been well studied. Next, it is necessary to study transient stability for the whole system. Under this situation, if the system is unstable in stage 2, under the conditions that the fault is cleared in time and before the CCT of the system, the system can still be stable.

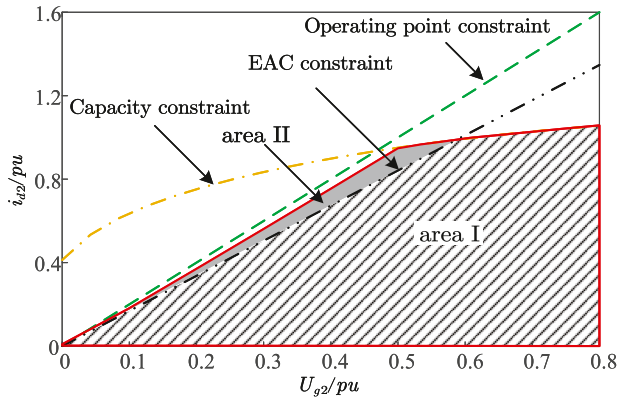

Fig. 10. Distribution of transient stable region on the i_{d2}-U_{g2} parameter plane including not only area I but also area II.

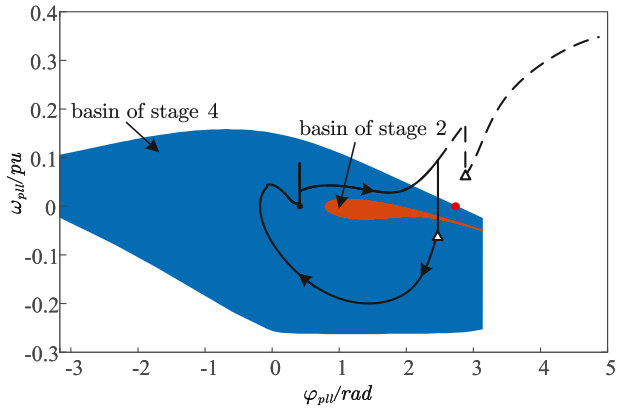

Fig. 11. Schematic shows of fault trajectory and stable region. The blue area and orange area represent the stable region in stages 4 and 2, respectively. The black solid line and black dashed line represent the stable and unstable trajectories, respectively. The triangle represents the position of φ_{pll} and ω_{pll} in the phase plane at the time of clearing fault.

As one example, Fig. 11 shows the phase trajectories of φ_{pll} and ω_{pll} for two different cases. U_g dips to 0.2 p.u. at $t_f = 0.1$ s. i_{d2} is set as 0.343 p.u. The fault is cleared at $t_c = 0.72$ s and 0.73 s, corresponding to the stable and unstable cases, respectively, and U_g recovers to 1 p.u. Clearly, their fault duration times $\Delta t_c = t_c - t_f$ are 0.62s and 0.63s, respectively. Among them, the blue area represents the stable region in stage 4 for the whole system, and the orange area represents the stable region in stage 2. Clearly the former is much wider. This probably comes from the big jump of the value of U_g, as schematically shown in Fig. 3. When the fault is cleared, if the values of φ_{pll} and ω_{pll} represented by triangle are within the blue area, the system can recover stability (black solid line), although they have already been out of the stable region of stage 2. Otherwise the system becomes unstable and goes to infinity (black dashed line). Therefore, even when the system is unstable in stage 2, if the fault duration time of stage 2 is shorter than the CCT, the system stability can also recover.

In addition, the CCTs with the variation of i_{d2} for three different values of $U_{g2} = 0.2$ p.u., 0.1 p.u., and 0 p.u. are calculated and shown in Fig. 12. It can be seen that for a fixed

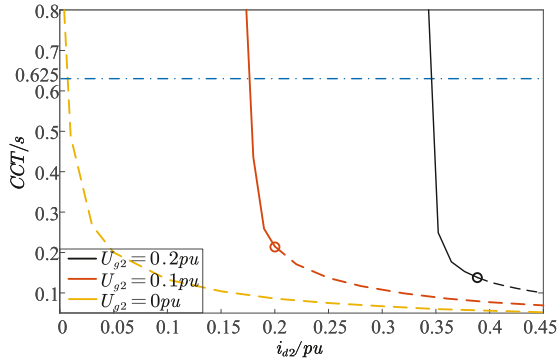

Fig. 12. Plots of CCT and i_{d2} under different U_{g2}'s. The dashed line indicates that the system has lost an operating point in stage 2 and the solid line indicates that the system has an operating point. The circle represents their boundary. The blue horizontal dot-dashed line indicates that the CCT is 625 ms.

U_{g2}, if i_{d2} is larger, the CCT becomes smaller. In addition, for a smaller U_{g2}, the corresponding i_{d2} also becomes much smaller. When i_{d2} is very small, the CCT goes to infinite. This means that for some particular cases, even if the fault is not cleared, the system can be stable. Except of all these, the solid line (dashed line) in Fig. 12 is used to indicate that the system has (no) operating point in stage 2, which are separated by a circle. Clearly as long as the CCT is larger than the maximum fault duration time, 625 ms, the system can still be stable. By considering this new effect, an additional gray area denoted by area II is superimposed in Fig. 10. It is notable that if the fault duration time is set as less than 625 ms, the area II can become larger and even exceed the operating point constraint. Clearly, both areas I and II surrounded by the red solid line in Fig. 10 constitute the whole transient stable region.

3) Simulation Verification: Two typical cases for either stable or unstable stage 2 will be addressed here. Set the fault as U_g dips to 0.2 p.u. at $t_f = 0.1$s and the PMSG switches to the TSC in stage 2.

Case I: To be compared with Fig. 9, in Fig. 13(a)–(c), the value of i_{d2} is set as 0.3 p.u., 0.35 p.u., and 0.42 p.u. respectively. At $t_c = 0.7$s, the fault is cleared and U_g recovers to 1 p.u. In Fig. 13(a), when i_{d2} is 0.3 p.u., φ_{pll} converges to a new steady state by multiple oscillations and the system recovers stability. In Fig. 13(b), if i_{d2} is 0.35 p.u., φ_{pll} diverges monotonously and the system eventually loses stability. In Fig. 13(c), when i_{d2} is 0.42 p.u., similarly φ_{pll} diverges monotonously with a much faster speed. These are perfectly consistent with the theoretical analysis in Fig. 9.

Case II: In Fig. 14(a) and (b), i_{d2} is fixed as 0.343 p.u. If the fault is cleared at $t_c = 0.72$ s in Fig. 14(a), although the system is unstable in stage 2, its stability eventually recovers. However, if the fault is cleared at $t_c = 0.73$ s in Fig. 14(b), the system remains unstable. Clearly now $t_c - t_f \approx \text{CCT} \approx 0.625s$, which is perfectly consistent with the theoretical analysis in Fig. 12.

C. Stage 3: Early Postfault

The main objective of stage 3 for the current climbing is to avoid large current disturbance. Here, the impact of k_{ramp} will be studied.

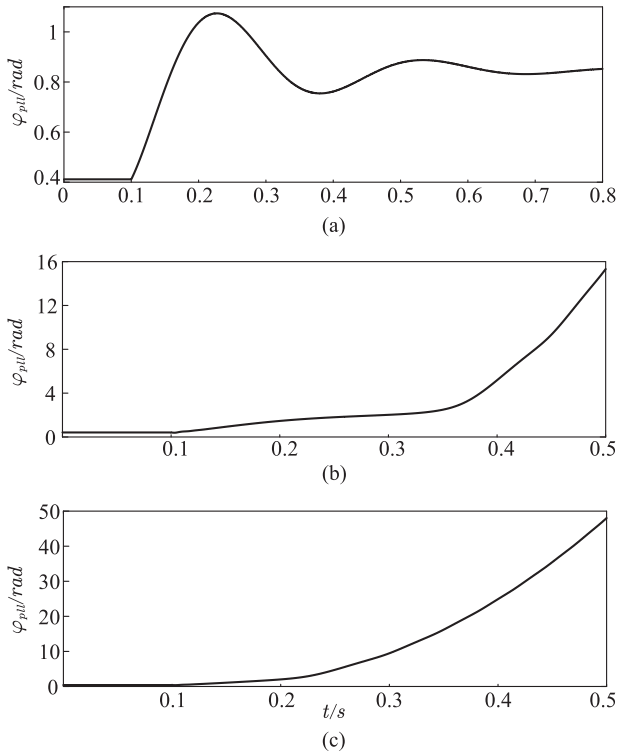

Fig. 13. Time domain simulations of φ_{pll} for case I. (a) $i_{d2} = 0.3$ p.u., (b) $i_{d2} = 0.35$ p.u., and (c) $i_{d2} = 0.42$ p.u. $t_f = 0.1$ s.

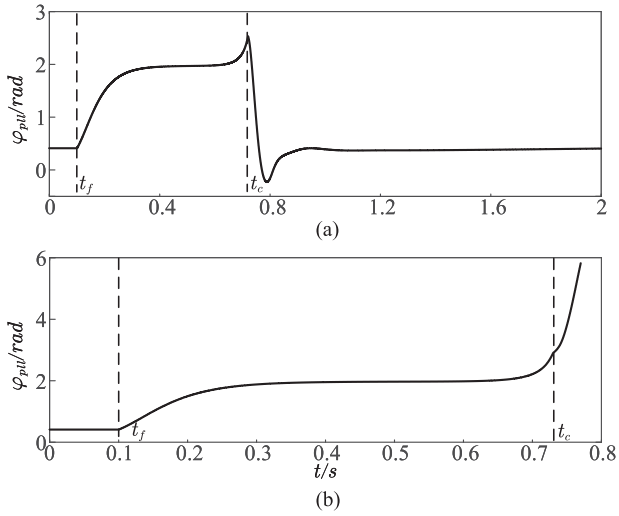

Fig. 14. Time domain simulations of φ_{pll} for case II. (a) $t_c = 0.72$ s and (b) $t_c = 0.73$ s. $t_f = 0.1$ s. $i_{d2} = 0.343$ p.u.

As shown in (17), the system is now nonautonomous in mathematics. As shown in Fig. 3(c), when i_{d3} climbs to the steady-state value of stage 1, the system will switch to the stage 4 control. Here, as $i_{d1} = 0.8$ p.u., the final value of i_{d3} is determined by 0.8 p.u. Meanwhile, the system trajectory in stage 3 depends on the final state in stage 2. By various case studies, it has been found that choosing any typical value of k_{ramp} does not change the system stability. For example, the system transient

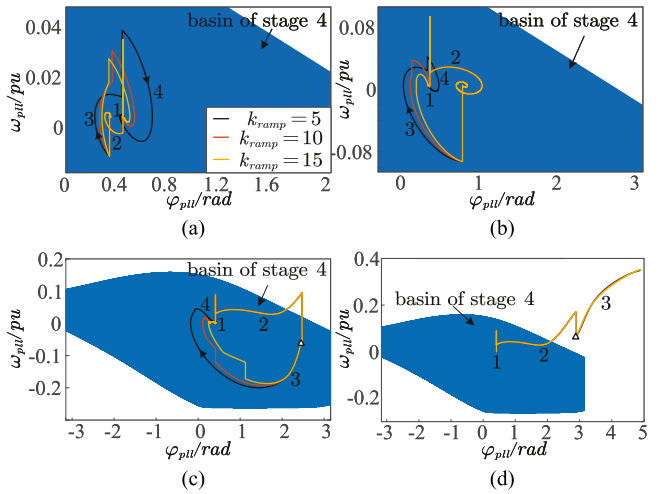

Fig. 15. Comparisons of fault trajectories and stable region of stage 4 for different k_{ramp}'s: $k_{\text{ramp}} = 5$, 10, or 15. (a) $U_{g2} = 0.5$ p.u., $i_{d2} = 0.3$ p.u., $t_f = 0.1$ s and $t_c = 0.7$ s. (b) $U_{g2} = 0.2$ p.u., $i_{d2} = 0.3$ p.u., $t_f = 0.1$ s and $t_c = 0.7$ s. (c) $U_{g2} = 0.2$ p.u., $i_{d2} = 0.343$ p.u., $t_f = 0.1$ s and $t_c = 0.72$ s. (d) $U_{g2} = 0.2$ p.u., $i_{d2} = 0.343$ p.u., $t_f = 0.1$ s and $t_c = 0.73$ s.

trajectories are shown in Fig. 15(a) and (b) for $U_{g2} = 0.5$ p.u. and 0.2 p.u., respectively. $i_{d2} = 0.3$ p.u., and k_{ramp}'s are 5, 10, or 15. It can be found that when the system is stable in stage 2, the transient trajectory is always within the stable region. This just corresponds to the case that the system is stable in stage 2, as shown in Fig. 13(a). Therefore, k_{ramp} does not change the system stability. In addition, the case in Fig. 14(a) is also studied that the system is unstable in stage 2 but finally it is stable in stage 4. Correspondingly, the transient trajectories are shown in Fig. 15(c) and (d) for $t_c = 0.72$ s and 0.73 s, respectively. $U_{g2} = 0.2$ p.u. and $i_{d2} = 0.343$ p.u., for k_{ramp}'s being 5, 10, or 15 again. Clearly if the system is unstable in stage 2, when the fault is cleared at $t_c = 0.72$s, the state denoted by the triangle is within the stable region, and the system is finally stable. However, if the fault is cleared at $t_c = 0.73$s, as the state is outside of the stable region, the system is finally unstable. Although the stage 3 trajectories change under different k_{ramp}'s, the initial states of stage 3 are fixed and their following trajectories do not change the system stability.

V. Experimental Verification

In order to verify the above observations, hardware-in-the-loop experiments are conducted based on the SpaceR. The SpaceR real-time simulation platform includes the host computer system, SpaceR, digital signal processing, and oscilloscope, as shown in Fig. 16. The SpaceR is a real-time simulation software, which consists of a real-time simulation machine and an PCI-E IO expansion box. In the experiment, the SpaceR simulates electromagnetic components such as power electronics and outputs measurement signals into the digital signal processing. Then, it feeds back the pulsewidth modulation signal to the SpaceR. The system model and parameters used in the experiment are the same as in Fig. 1 and Table I, respectively.

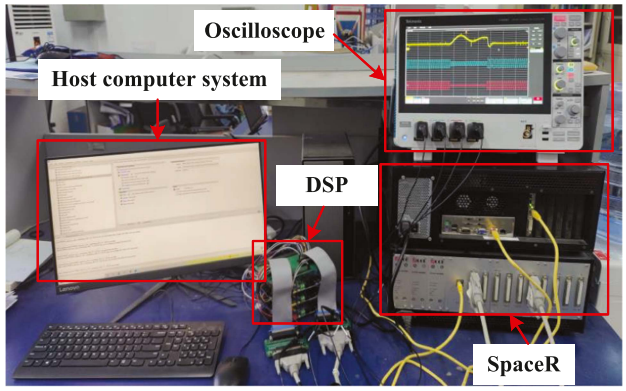

Fig. 16. SpaceR real-time simulation platform.

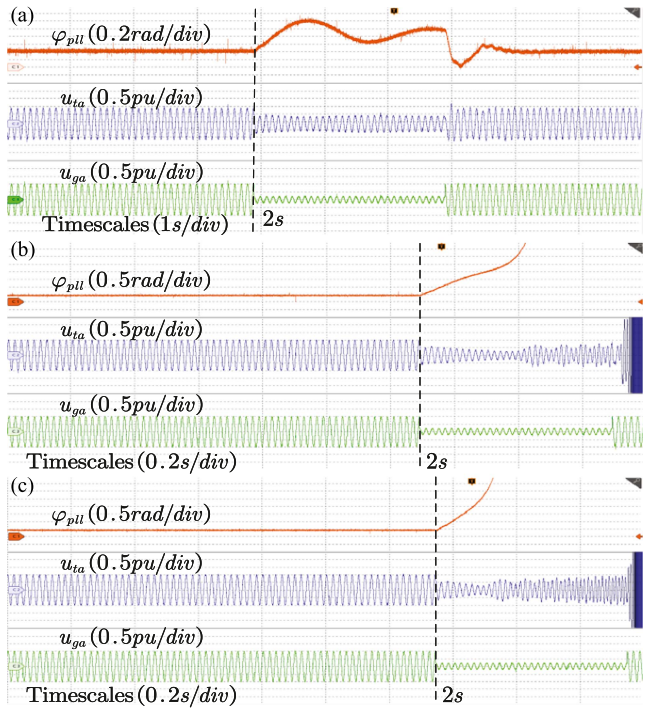

Fig. 17. Experimental results focusing on stage 2 for case I, to be compared with Fig. 13.

A. Stage 2: During-Fault

Four groups of comparative experiments are set up to verify the correctness of the above analyses for Cases I–IV.

Case I: At $t_f = 2$s, U_g dips to 0.2 p.u., and at $t_c = 2.6$s, U_g recovers to 1.0 p.u. The experimental results are shown in Fig. 17(a)–(c) for i_{d2} being 0.3 p.u., 0.35 p.u., and 0.42 p.u., respectively. It is clear that as i_{d2} is 0.3 p.u., φ_{pll} converges with multiple oscillations and the system is stable. When i_{d2} is 0.35 p.u., φ_{pll} monotonically diverges and the system is unstable. When i_{d2} is 0.42 p.u., φ_{pll} monotonically diverges again, but shows a much faster speed. They are consistent with the simulation results in Fig. 13.

Case II: When $t_f = 2$ s, U_g dips to 0.2 p.u. and $i_{d2} = 0.343$ p.u. At the fault clearing time t_c, again U_g recovers to 1 p.u.

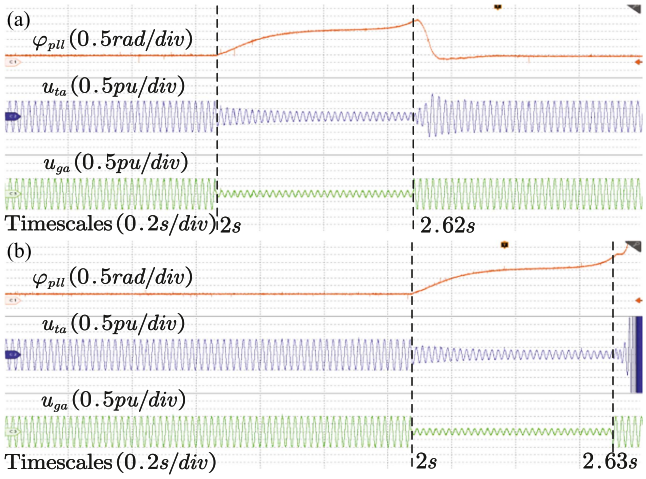

Fig. 18. Experimental results focusing on stage 2 for case II, to be compared with Fig. 14.

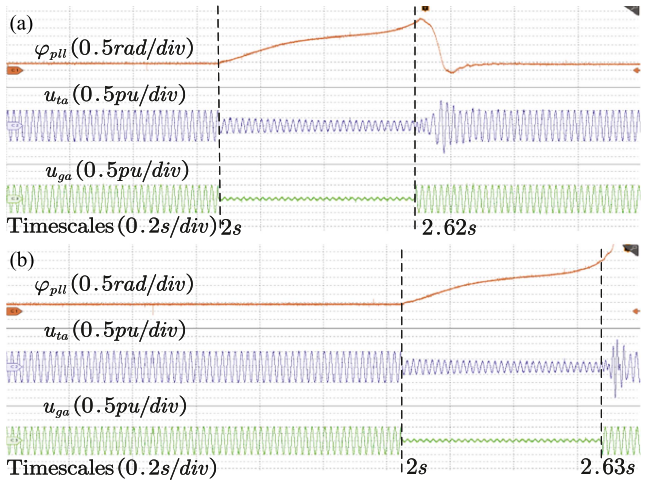

Fig. 19. Experimental results focusing on stage 2 for case III.

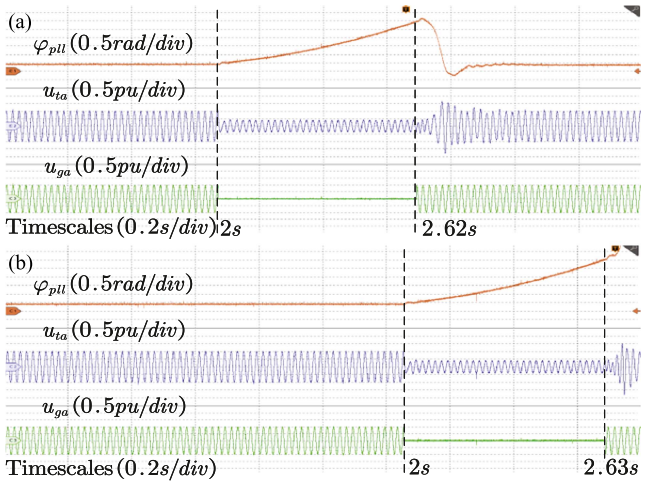

Fig. 20. Experimental results focusing on stage 2 for case IV.

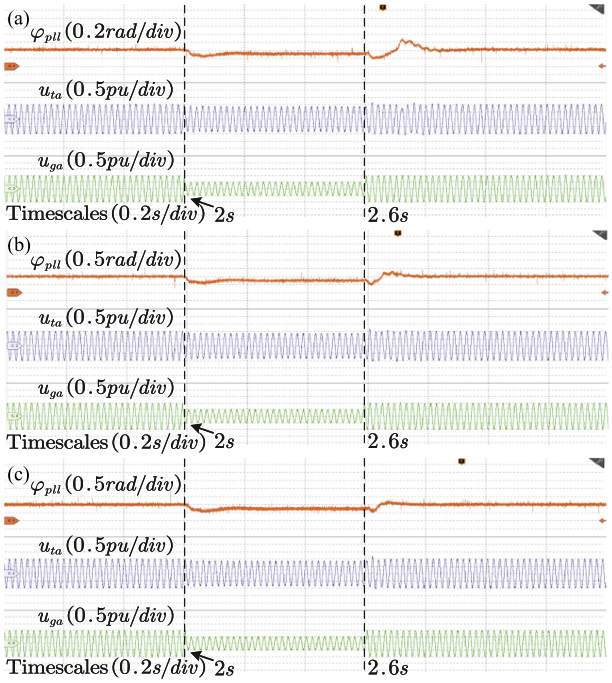

Fig. 21. Experimental results focusing on stage 3 for case I, to be compared with Fig. 15(a).

The experimental results in Fig. 18(a) and (b) are for the fault clearing times being $t_c = 2.62$ s and 2.63 s, respectively. When the fault is cleared at 2.62 s, although φ_{pll} is unstable in stage 2, the system eventually recovers to be stable. However, when the fault is cleared at 2.63 s, the system becomes unstable. This is also well consistent with the simulation results in Fig. 14.

Case III: When $t_f = 2$ s, U_g dips to 0.1 p.u. and $i_{d2} = 0.171$ p.u. The experimental results in Fig. 19(a) and (b) are for the fault clearing times being $t_c = 2.62$ s and 2.63 s, respectively. When the fault is cleared at 2.62 s, although φ_{pll} is unstable in stage 2, the system eventually recovers to be stable. However, when the fault is cleared at 2.63 s, the system becomes unstable. At the same time, in Fig. 12, when $U_{g2} = 0.1$ p.u. and $i_{d2} = 0.171$ p.u., the CCT of the system is 625 ms. When $t_c - t_f <$ 625 ms, the system is stable, and oppositely when $t_c - t_f >$ 625 ms, the system is unstable. Hence, the experimental results are consistent with the analyses.

Case IV: When $t_f = 2$ s, U_g dips to 0 p.u. and $i_{d2} = 0.007$ p.u. The experimental results in Fig. 20(a) and (b) are for the fault clearing times being $t_c = 2.62$ s and 2.63 s, respectively. When the fault is cleared at 2.62 s, although φ_{pll} is unstable in stage 2, the system eventually recovers to be stable. However, when the fault is cleared at 2.63 s, the system becomes unstable. At the same time, in Fig. 12, when $U_{g2} = 0$ p.u. and $i_{d2} = 0.007$ p.u., the CCT of the system is 625 ms. When $t_c - t_f <$ 625 ms, the system is stable. When $t_c - t_f >$ 625 ms, the system is unstable. Hence, the experimental results are consistent with the analyses.

Clearly all these comparative results in the experiments demonstrate that the two transient stability scenarios are typical, for either it is stable solely in stage 2, or it is unstable in stage 2 but becomes stable finally in stage 4.

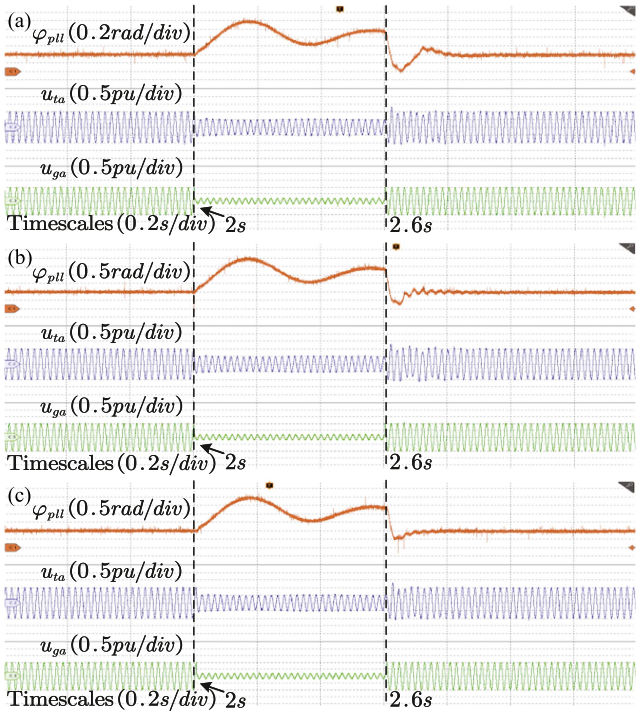

Fig. 22. Experimental results focusing on stage 3 for case II, to be compared with Fig. 15(b).

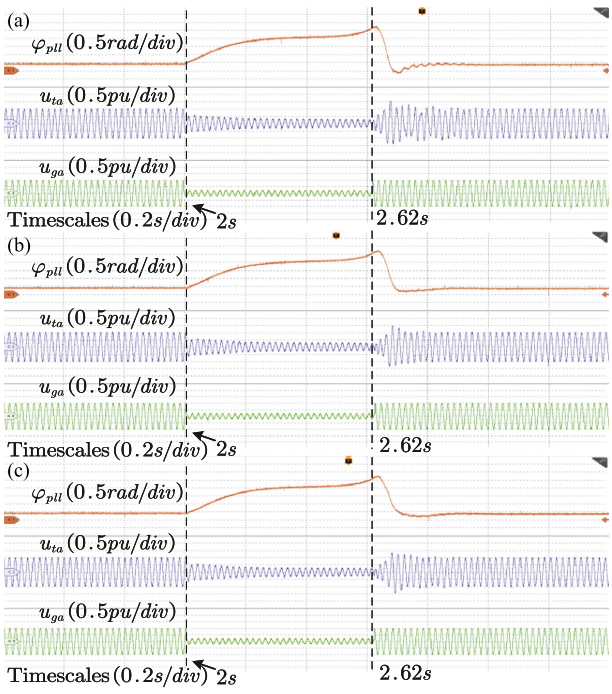

Fig. 23. Experimental results focusing on stage 3 for case III, to be compared with Fig. 15(c).

B. Stage 3: Early Postfault

Four groups of comparative experiments are set up to verify the correctness of the above analyses for Cases I–IV.

Case I: At $t_f = 2$ s, U_g dips to 0.5 p.u., $i_{d2} = 0.3$ p.u. and at $t_c = 2.6$ s, U_g recovers to 1.0 p.u. The experimental results are shown in Fig. 21(a)–(c) for k_{ramp} being 5, 10, and 15, respectively. It can be found that when the system is stable in stage 2, it is stable after clearing the fault. The transient stability of the system does not change with the change of k_{ramp}. Therefore, k_{ramp} does not change the system stability. This is well consistent with Fig. 15(a).

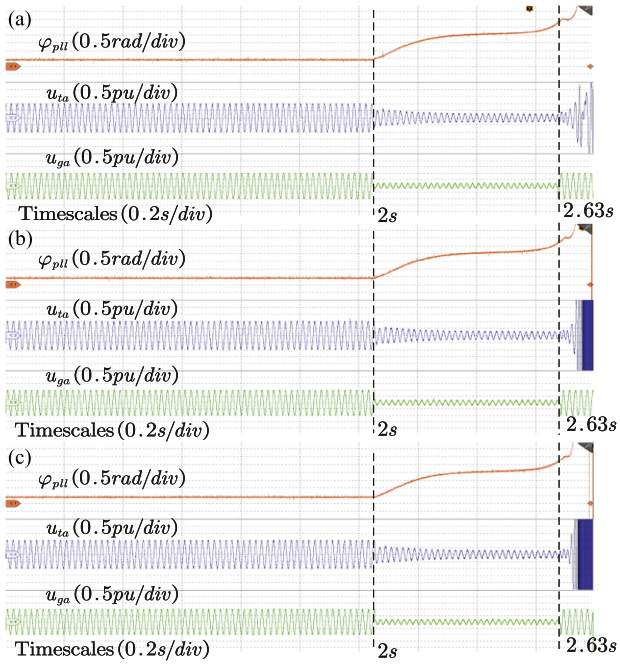

Fig. 24. Experimental results focusing on stage 3 for case IV, to be compared with Fig. 15(d).

Case II: At $t_f = 2$ s, U_g dips to 0.2 p.u., $i_{d2} = 0.3$ p.u. and at $t_c = 2.6$ s, U_g recovers to 1.0 p.u. The experimental results are shown in Fig. 22(a)–(c) for k_{ramp} being 5, 10, and 15, respectively. It can be found that when the system is stable in stage 2, it is stable after clearing the fault. The transient stability of the system does not change with the change of k_{ramp}. Therefore, k_{ramp} does not change the system stability. This is also well consistent with the Fig. 15(b).

Case III: At $t_f = 2$ s, U_g dips to 0.2 p.u., $i_{d2} = 0.343$ p.u. and at $t_c = 2.62$ s, U_g recovers to 1.0 p.u. The experimental results are shown in Fig. 23(a)–(c) for k_{ramp} being 5, 10, and 15, respectively. It can be found that although the system is unstable in stage 2, it is stable after clearing the fault at $t_c = 2.62$ s. The transient stability of the system does not change with the change of k_{ramp}. Therefore, k_{ramp} does not change the system stability. This is also well consistent with the Fig. 15(c).

Case IV: At $t_f = 2$ s, U_g dips to 0.2 p.u., $i_{d2} = 0.343$ p.u. and at $t_c = 2.63$ s, U_g recovers to 1.0 p.u. The experimental results are shown in Fig. 24(a)–(c) for k_{ramp} being 5, 10, and 15, respectively. It can be found that when the system is unstable in stage 2, it is unstable after clearing the fault at $t_c = 2.63$ s. The transient stability of the system does not change with the change of k_{ramp}. Therefore, k_{ramp} does not change the system stability. This is also well consistent with the Fig. 15(d).

Clearly all these comparative results in the experiments demonstrate that although the trajectories for different values

of k_{ramp} change, the initial states of stage 3 are fixed and their following trajectories do not change the stability.

VI. Conclusion

In conclusion, this article divides the transient process of the PMSG grid-connected system with the TSC into four different stages, establishes the corresponding simplified mechanism models and the associated machine–network interface relations for each stage, and uncovers the influence of major parameters on the system transient stability. It is found that for the system transient stability, it can be stable in stage 2, or it can also be unstable in stage 2 but become stable with a fast fault cut. Therefore, the transient stable region can be wider than researchers previously thought, in terms of system transient stability including the whole four stages. The transient stability in stage 2 is only a sufficient condition, but not a necessary condition. This is quite different from most of previous studies focusing solely on the stability of stage 2. This article provides a panoramic view for the transient stability of the PMSG grid-connected system. It significantly catches the bulk dynamical behaviors and establishes a systematical picture for the entire transient process. All these studies could provide a theoretical basis for engineering applications.

VII. Discussions

In the end, it is necessary to give some discussions.

1) As we know, most of previous studies focused only on the dynamics of stage 2. Even lack of operating point on this stage is believed as loss of synchronization and closely connected with the system stability. In this article, it is uncovered that the transient stability on stage 2 is only a sufficient condition, but not a necessary condition, and actually the system can be stable under wider parameter regions. Now, the relation between stage 2 and other stages, and its stability on this stage and the whole system, etc. become clear. Different from the already-existing sliced incomplete studies focusing on the sole stage 2 [23], [43], [44], [45], here all TSCs are considered in a systematical manner. This can be believed as one of the most contributions of this article.
2) The basis for the model simplification in this article is the singular perturbation theory in mathematics [46] or the enslaving principle in the Haken's synergetics in physics [47]. Only the slow-scale dynamics are dominant, as all fast-scale will naturally damp in transient. This is exactly what we can see in Fig. 5. In addition, as the PLL dynamics are always important for synchronization in all four stages, their equations in the transient stability analysis have to be maintained. Next, it is interesting to compare with the two recent works considering the switching controls of converter systems in [30] and [31]. Their distinctions are clear. In [30], it establishes a transient model of VSC grid-connected system considering TSC and analyzes the expression of discontinuous variables after switching. However, it only provides a detailed modeling and does not reveal the transient stability mechanism. At the same time, it does not consider the climbing control and machine-side dynamics, which are important for the PMSG. In [31], it simplifies the transient model of the VSC grid-connected system with the TSC into a second-order PLL model with the virtual torque, inertia, and damping, and then proposes the stability criterion by the EAC in a unified form. The model assumes that the active/reactive power control loops belong to the electromechanical timescale, such that the current instructions can be approximately obtained through algebraic equations. It considers the active/reactive power control loops and PLL only, and it does not consider the machine-side dynamics and all voltage outer control loops of the GSC, such as the DVC and TVC. In addition, it considers five stages, including the prefault stage, fault dead-time stage, fault-during stage, fault recovery dead-time stage, and postfault stage, and it does not consider the early post-fault stage 3 for the climbing control, which is also important for the PMSG. Clearly, the second-order sequential model in [31] is comparatively simpler, to be applied with the EAC analysis. With all the TSC effects considered in this article, the model is no longer a simple second-order system in stages 1, 3, and 4, but high-dimensional nonlinear systems, as shown in (9) for stages 1 and 4, and (17) for stage 3. Hence the EAC is no longer applicable. Except all these, the existence of equilibrium point on stage 2 is used as one criterion for the transient stability [31], which is also completely different from the result in this article.
3) Finally, it is also interesting to compare transient stability of the PMSG system with that of the SG system [40]. Although the basic condition for the transient stability is the same in mathematics, there are many distinctions in detail. For instance, usually for the SG, it has three different stages including prefault, during-fault, and post-fault. In each stage, usually the dynamical equations are the same, but with different parameters. The key variables for the (synchronous) rotor angle and its speed are always continuous. Here, with the TSCs in the LVRT, the transient dynamics becomes much more complicated. The system exhibits four different stages including prefault, during-fault, early postfault, and postfault accordingly. Not only the parameters but also dynamical equations can be completely different. In addition, although the key variables in the transient are determined by the PLL phase and frequency outputs, φ_{pll} and ω_{pll}, ω_{pll} can show discontinuity in each switch. Moreover, this hybrid switching dynamical system can exhibit not only electromechanical-dominant, but also electromagnetic-dominant behaviors under different stages. Clearly our mechanism model in this article establishes a closer connection with the transient stability of the SG system in a systematical way.

Appendix

For additional model verification, Figs. 25 and 26 show the simulation comparison results between the simplified model and

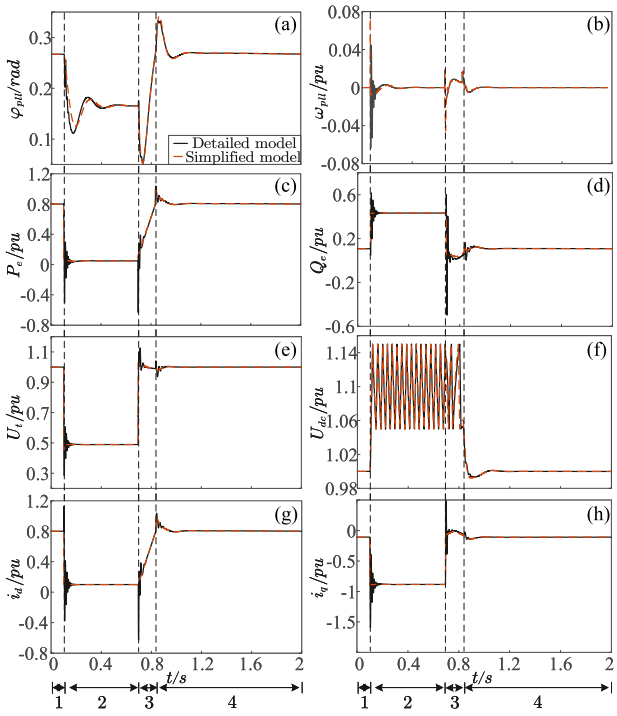

Fig. 25 (a)–(h) Simulation comparisons of the simplified and detailed models after faults for φ_{pll}, ω_{pll}, P_e, Q_e, U_t, U_{dc}, i_d, and i_q, respectively, when the SCR is 3.

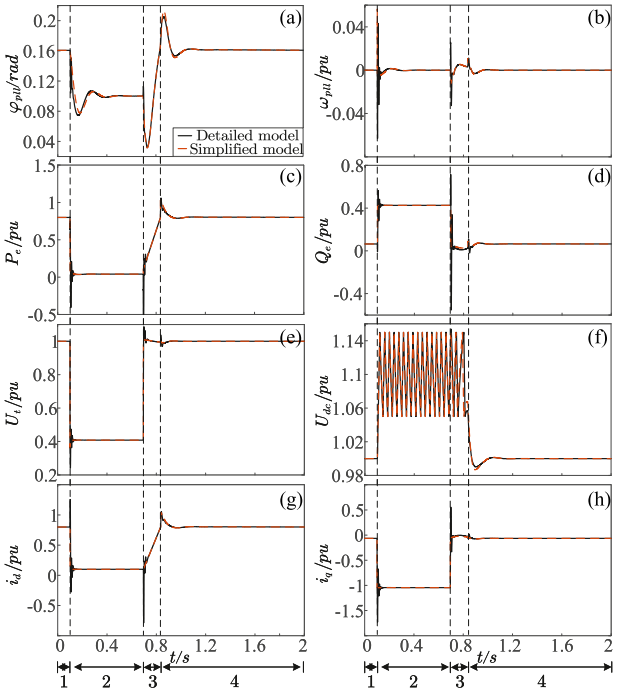

Fig. 26 (a)–(h) The same as Fig. 1, but for the SCR being 5, instead.

the detailed electromagnetic model of the PMSG grid-connected system with the TSC when the SCR is 3 and 5, respectively. At $t_f = 0.1$ s, the infinite-bus voltage U_g dips to 0.2 p.u. At $t_c = 0.7$ s, the fault is cleared and U_g recovers to 1 p.u. For the fault duration time, $t_c - t_f = 0.6$ s. It can be seen that they fit well in all transient stages, except some high-frequency oscillations.

REFERENCES

[1] N. D. Hatziargyriou, J. V. Milanovic, C. Rahmann, V. Ajjarapu, and C. Vournas, "Stability definitions and characterization of dynamic behavior in systems with high penetration of power electronic interfaced technologies," Tech. Rep., 2020.

[2] Y. Gu and T. C. Green, "Power system stability with a high penetration of inverter-based resources," *Proc. IEEE*, vol. 111, no. 7, pp. 832–853, Jul. 2023.

[3] R. Ma, Y. Zhang, Z. Yang, J. Kurths, M. Zhan, and C. Lin, "Synchronization stability of power-grid-tied converters," *Chaos*, vol. 33, no. 3, 2023, Art. no. 0 32102.

[4] "Code on security and stability for power system," (*in Chinese*) Tech. Rep., 2020.

[5] R. Ma, Y. Zhang, M. Han, J. Kurths, and M. Zhan, "Synchronization stability and multi-timescale analysis of renewable-dominated power systems," *Chaos*, vol. 33, no. 8, 2023, Art. no. 0 82101.

[6] Y. Zhang, M. Han, and M. Zhan, "The concept and understanding of synchronous stability in power electronic-based power systems," *Energies*, vol. 16, no. 6, 2023, Art. no. 2923.

[7] A. Nair, S. Kamalasadan, J. Geis-Schroer, S. Patel, and M. Smith, "An investigation of grid stability and a new design of adaptive phase-locked loop for wind-integrated weak power grid," *IEEE Trans. Ind. Appl.*, vol. 58, no. 5, pp. 5871–5884, May 2022.

[8] S. Ghosh, M. K. Bakhshizadeh, G. Yang, 5. B. C. Kocewiak Pal, and M. Nadarajah, "Nonlinear stability investigation of type-4 wind turbines with non-autonomous behavior based on transient damping characteristics," *IEEE Access*, vol. 11, pp. 76059–76070, 2023.

[9] H. Yuan, H. Xin, L. Huang, Z. Wang, and D. Wu, "Stability analysis and enhancement of type-4 wind turbines connected to very weak grids under severe voltage sags," *IEEE Trans. Energy Convers.*, vol. 34, no. 2, pp. 838–848, Feb. 2019.

[10] D. Gautam, V. Vittal, and T. Harbour, "Impact of increased penetration of DFIG-based wind turbine generators on transient and small signal stability of power systems," *IEEE Trans. Power Syst.*, vol. 24, no. 3, pp. 1426–1434, Mar. 2009.

[11] E. Vittal, M. O'Malley, and A. Keane, "Rotor angle stability with high penetrations of wind generation," *IEEE Trans. Power Syst.*, vol. 27, no. 1, pp. 353–362, Jan. 2011.

[12] L. Meegahapola and D. Flynn, "Impact on transient and frequency stability for a power system at very high wind penetration," in *Proc. IEEE PES Gen. Meeting*, 2010, pp. 1–8.

[13] P. Mu, D. Zhao, and J. Wang, "Influence mechanism analysis of large-scale wind power integration on power system angle stability," (*in Chinese*) *Proc. CSEE*, vol. 37, no. 5, pp. 1324–1332, 2017.

[14] L. Chen, Y. Min, Y. Dai, and M. Wang, "Stability mechanism and emergency control of power system with wind power integration," *IET Renewable Power Gener.*, vol. 11, no. 1, pp. 3–9, 2017.

[15] Z. Liu, "Research on transient stability of power system integrated with PMSGs," (*in Chinese*) Ph.D. dissertation, School of Electrical and Electronic Engineering, 2016.

[16] M. G. Taul, X. Wang, P. Davari, and F. Blaabjerg, "An overview of assessment methods for synchronization stability of grid-connected converters under severe symmetrical grid faults," *IEEE Trans. Power Electron.*, vol. 34, no. 10, pp. 9655–9670, Oct. 2019.

[17] M. Huang, Y. Peng, K. T. Chi, Y. Liu, J. Sun, and X. Zha, "Bifurcation and large-signal stability analysis of three-phase voltage source converter under grid voltage dips," *IEEE Trans. Power Electron.*, vol. 32, no. 11, pp. 8868–8879, Nov. 2017.

[18] C. He, X. He, H. Geng, H. Sun, and S. Xu, "Transient stability of low-inertia power systems with inverter-based generation," *IEEE Trans. Energy Convers.*, vol. 37, no. 4, pp. 2903–2912, Apr. 2022.

[19] X. Fu et al., "Large-signal stability of grid-forming and grid-following controls in voltage source converter: A comparative study," *IEEE Trans. Power Electron.*, vol. 36, no. 7, pp. 7832–7840, Jul. 2021.

[20] Z. Wang et al., "PLL synchronization transient stability analysis of a weak-grid connected VSC during asymmetric faults," *IEEE Trans. Power Electron.*, vol. 39, no. 2, pp. 2140–2154, Feb. 2024.

[21] M. Zarif Mansour, S. Me, S. Hadavi, B. Badrzadeh, A. Karimi, and B. Bahrani, "Nonlinear transient stability analysis of phased-locked loop-based grid-following voltage-source converters using lyapunov's direct method," *IEEE J. Emerg. Sel. Topics Power Electron.*, vol. 10, no. 3, pp. 2699–2709, Mar. 2022.
[22] Y. Zhang, C. Zhang, and X. Cai, "Large-signal grid-synchronization stability analysis of PLL-based VSCs using lyapunov's direct method," *IEEE Trans. Power Syst.*, vol. 37, no. 1, pp. 788–791, Jan. 2021.
[23] R. Ma, J. Li, J. Kurths, S. Cheng, and M. Zhan, "Generalized swing equation and transient synchronous stability with PLL-based VSC," *IEEE Trans. Energy Convers.*, vol. 37, no. 2, pp. 1428–1441, Feb. 2022.
[24] X. Li, Z. Tian, X. Zha, P. Sun, Y. Hu, and M. Huang, "An iterative equal area criterion for transient stability analysis of grid-tied converter systems with varying damping," *IEEE Trans. Power Syst.*, vol. 39, no. 1, pp. 1771–1784, Jan. 2023.
[25] H. Wu and X. Wang, "Design-oriented transient stability analysis of PLL-synchronized voltage-source converters," *IEEE Trans. Power Electron.*, vol. 35, no. 4, pp. 3573–3589, Apr. 2020.
[26] Q. Hu, L. Fu, F. Ma, G. Wang, C. Liu, and Y. Ma, "Impact of LVRT control on transient synchronizing stability of PLL-based wind turbine converter connected to high impedance AC grid," *IEEE Trans. Power Syst.*, vol. 38, no. 6, pp. 5445–5458, Jun. 2023.
[27] Z. Wang, G. Zhu, H. Wu, X. Gao, L. Ding, and X. Wang, "Current reference control scheme of voltage source converters to ensure the existence of stable equilibrium points during grid fault," *IEEE Trans. Power Electron.*, vol. 38, no. 9, pp. 10750–10765, Sep. 2023.
[28] Y. Li, Y. Tang, Y. Lu, F. Hua, and Z. Du, "Synchronization stability of grid-connected VSC with limits of PLL," *IEEE Trans. Power Syst.*, vol. 38, no. 4, pp. 3965–3976, Apr. 2022.
[29] Y. Zhang and M. Zhan, "Transient synchronization stability mechanism of PMSG with additional inertia control," *IET Renewable Power Gener.*, vol. 18, pp. 2773–2784, 2024.
[30] W. Ding, H. Geng, B. Ren, Q. Li, and R. Sun, "Analytical switching modeling method of grid-connected converters for transient stability analysis," *IEEE Trans. Ind. Appl.*, vol. 60, no. 5, pp. 7511–7521, May 2024.
[31] J. Pei, J. Yao, Y. Liu, S. Chen, P. Sun, and S. Huang, "Modeling and transient synchronization stability analysis for PLL-based renewable energy generator considering sequential switching schemes," *IEEE Trans. Power Electron.*, vol. 37, no. 2, pp. 2165–2179, Feb. 2022.
[32] A. Ellis, Y. Kazachkov, E. Muljadi, P. Pourbeik, and J. Sanchez-Gasca, "Description and technical specifications for generic WTG models: A status report," in *Proc. IEEE/PES Power Syst. Conf. Expo.*, 2011, pp. 1–8.
[33] K. Clark, N. W. Miller, and J. J. Sanchez-Gasca, "Modeling of GE wind turbine-generators for grid studies," Tech. Rep., 2010.
[34] P. Pourbeik, "Proposed changes to the WECC WT3 generic model for type-3 wind turbine generators," Tech. Rep. 16, 2013.
[35] D. Sun et al., "Effect of the low voltage ride through characteristics on PMSG terminal transient voltage in weakly-synchronized gird," (*in Chinese*) *Proc. CSEE*, vol. 41, no. 14, pp. 4777–4786, 2021.
[36] G. Abad, J. Lopez, M. Rodriguez, L. Marroyo, and G. Iwanski, *Doubly Fed Induction Machine: Modeling and Control for Wind Energy Generation*. Hoboken, NJ, USA: Wiley, 2011.
[37] R. Teodorescu, M. Liserre, and P. Rodriguez, *Grid Converters for Photovoltaic and Wind Power Systems*. Hoboken, NJ, USA: Wiley, 2011.
[38] S. P. Me, S. Zabihi, F. Blaabjerg, and B. Bahrani, "Adaptive virtual resistance for postfault oscillation damping in grid-forming inverters," *IEEE Trans. Power Electron.*, vol. 37, no. 4, pp. 3813–3824, Apr. 2021.
[39] Z. Yang, R. Ma, S. Cheng, and M. Zhan, "Nonlinear modeling and analysis of grid-connected voltage-source converters under voltage dips," *IEEE J. Emerg. Sel. Topics Power Electron.*, vol. 8, no. 4, pp. 3281–3292, Apr. 2020.
[40] P. Kundur, *Power System Stability and Control*. New York, Ny, USA: McGraw Hill, 1994.
[41] Y. Zhang and M. Zhan, "Dominant transient unstable characteristics of PLL-based grid-connected converters," (*in Chinese*) *Proc. CSEE*, vol. 43, no. 23, pp. 9285–9296, 2023.
[42] R. Ma et al., "Dominant transient equations of grid-following and grid-forming converters by controlling-unstable-equilibrium-point-based participation factor analysis," *IEEE Trans. Power Syst.*, vol. 39, no. 3, pp. 4818–4834, Mar. 2024.
[43] Ö. Göksu, R. Teodorescu, C. L. Bak, F. Iov, and P. C. Kjær, "Instability of wind turbine converters during current injection to low voltage grid faults and PLL frequency based stability solution," *IEEE Trans. Power Syst.*, vol. 29, no. 4, pp. 1683–1691, Apr. 2014.
[44] Y. Yang, D. Zhu, D. Zhou, X. Zou, J. Hu, and Y. Kang, "Synchronization instability mechanism and damping enhancement control for DFIG-based wind turbine during grid faults," *IEEE Trans. Power Electron.*, vol. 38, no. 10, pp. 12104–12115, Oct. 2023.
[45] Y. Zhang, M. Cheng, M. Zhan, J. Yu, Y. Zhu, and M. Wu, "LVRT during-fault-stage equilibrium point is unnecessary for renewable grid-tied systems," in *Proc. 4th Power Syst. Green Energy Conf.*, 2024, pp. 941–946.
[46] E. Shchepakina, V. Sobolev, and M. P. Mortell, *Singular Perturbations: Introduction to System Order Reduction Methods With Applications*. Berlin, Germany: Springer, 2014.
[47] H. Haken, *Synergetics*. Berlin, Germany: Springer, 1977.

Yayao Zhang received the B.S. degree in electrical engineering from Hunan University, Changsha, China, in 2020. He is currently working toward the Ph.D. degree in electrical engineering with the School of Electrical and Electronic Engineering, Huazhong University of Science and Technology, Wuhan, China.

His research interests include the transient stability of renewable dominated power systems.

Meng Zhan (Senior Member, IEEE) was born in Jingdezhen City, Jiangxi Province, China, in 1974. He received the B.S. degree in physics, in 1996, and the Ph.D. degree in nonlinear physics, in 2001, both from Beijing Normal University, Beijing, China.

He was a postdoc Researcher with the National University of Singapore, Singapore, and University of Toronto, Canada, from 2001 and 2006. After working as a Full Professor with the Wuhan Institute of Physics and Mathematics, the Chinese Academy of Sciences, from 2006 and 2015, recently he joined in the State Key Laboratory of Advanced Electromagnetic Engineering and Technology, and School of Electrical and Electronic Engineering, Huazhong University of Science and Technology. He has long been engaged in the study of nonlinear dynamics theory of complex systems in multiple directions, such as coupled nonlinear systems, chaos synchronization and control, pattern formation, and complex network dynamics. He has authored or coauthored over 100 SCI papers in internationally peer-reviewed journals. His research interests include power system stability, power-electronics-based power system dynamics, and nonlinear analysis of power system.